

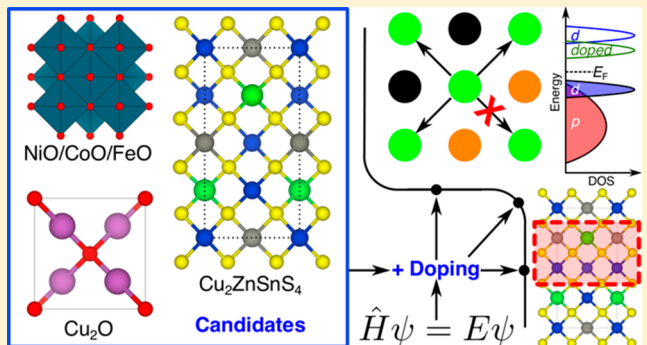
Novel Solar Cell Materials: Insights from First-Principles

Gopalakrishnan Sai Gautam,[†] Thomas P. Senftle,^{†,II} Nima Alidoust,^{‡,I} and Emily A. Carter^{*,§}

[†]Department of Mechanical and Aerospace Engineering, [‡]Department of Electrical Engineering, and [§]School of Engineering and Applied Science, Princeton University, Princeton, New Jersey 08544-5263, United States

Supporting Information

ABSTRACT: Although silicon solar cells currently dominate the market share for photovoltaic (PV) devices, it is important to explore other materials and device configurations that could be cheaper and more environmentally friendly to produce, as well as potentially more efficient at energy conversion. Here, we review some of our recent theoretical work aimed at accurate evaluation of key materials properties associated with optimizing alternative PV materials. These include potential new light absorbers and transparent conductors in devices ranging from traditional PVs to tandem dye-sensitized solar cells and thin-film PVs to intermediate band gap PVs. We specifically focus on two materials families: transition-metal oxides (TMOs), such as NiO, CoO, FeO, and Cu₂O, and mixed metal sulfides, such as Cu₂ZnSnS₄. Both families are p-type semiconductors being explored as less expensive solar cell components.



1. INTRODUCTION

Harvesting solar energy by converting incoming radiation into usable electricity via photovoltaic (PV) technology is a crucial component of any strategy to ensure a sustainable, fossil-fuel-free future. While multiple solar cell designs have been designed and prototyped, crystalline silicon (Si) still dominates commercial technology as the base semiconductor in a single-junction device (Figure 1a).^{1,2} However, the performance of Si PVs is limited by the intrinsic electronic properties of Si, such as its indirect band gap that inhibits light absorption and its less than optimal band gap.³ Also, the efficiency of any single-junction solar cell is bounded by the Shockley–Queisser (SQ) limit,⁴ which sets the maximum efficiency of the conversion of solar energy to electricity to ~33.14%. Exploring new candidate semiconductors and alternative device designs therefore is important for both reducing costs and improving efficiencies.

A pathway to improve efficiency and reduce the cost of current Si single-gap devices is to design novel semiconductors that can overcome the intrinsic limitations of bulk Si.³ The poor light absorption in Si PVs typically is compensated for by using thicker absorber layers in the cell. However, manufacturing less-efficient solar cells consumes more energy and materials for a given power output (the semiconductor itself and ancillary materials for wiring, coating, etc.), increasing the cost of production. Moreover, Si's band gap of 1.1 eV is less than ideal, reducing power output. It therefore is still important to develop alternative semiconductors that enable sustainable, efficient, “thin-film” PV devices. Such semiconductors will (i) have direct band gaps (to enhance light absorption), close to the SQ “ideal” PV gap of ~1.5 eV⁴ (to maximize power

output); (ii) be comprised of abundant, nontoxic, and inexpensive-to-process materials; (iii) exhibit low carrier-recombination rates (to ensure separation of photogenerated electron–hole pairs); (iv) yield sufficient currents via highly mobile carriers (i.e., fewer traps); and (v) be stable under synthesis and operating conditions (e.g., no performance-limiting defects or impurities). Several direct-band-gap materials, including GaAs, CdTe, Cu(In,Ga)(S,Se)₂, and Pb-based perovskites,^{6–11} have been identified and in some cases commercialized as high-efficiency, single-gap devices. However, these technologies use either rare and/or toxic constituents and hence do not represent a fully sustainable alternative to Si PVs when their entire life cycle is considered.

Alternative device designs that theoretically can exceed the SQ limit have been explored, including multijunction PV cells (MJVP, Figure 1b)¹² and intermediate band gap PV cells (IBPV, Figure 1c).¹³ MJVPs stack semiconductors of different band gaps to maximize energy conversion, enabling absorption of photons with multiple minimum energies ($\hbar\nu_1$, $\hbar\nu_2$, $\hbar\nu_3$ in Figure 1b). Several MJVPs employ III–V semiconductors, such as (In,Ga)P, (In,Ga)As, and Ga(As,Sb), with band gaps tuned¹⁴ to different sunlight wavelengths. Although each individual semiconductor still is bound by the SQ limit, arranging the absorbing materials with decreasing band gaps (from outermost to innermost layers) dramatically increases the overall light absorption of the cell, thereby increasing its efficiency. An infinite number of individual semiconductors

Received: August 22, 2018

Revised: October 12, 2018

Published: October 17, 2018

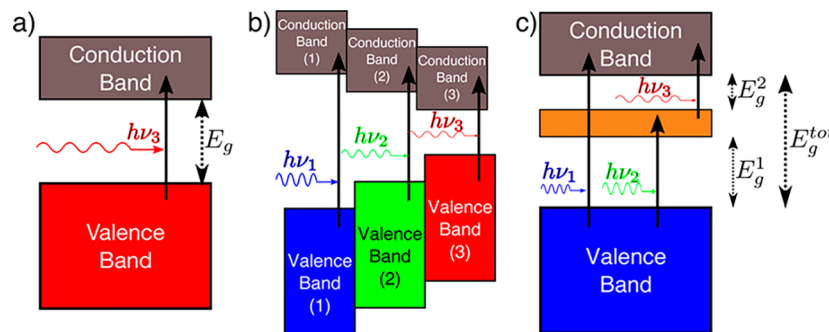


Figure 1. Typical light absorption mechanisms in (a) single-gap, single-junction cell; (b) multijunction, tandem cell; and (c) intermediate-band semiconductors. Adapted from ref 5. Copyright 2016 American Institute of Physics.

stacked in a multijunction configuration theoretically could achieve an efficiency as high as 86.8%.¹⁵

In the case of IBPVs, the cell design employs in a single-junction device an intermediate band semiconductor (IBSC; Figure 1c) that exhibits a narrow, partially filled band intermediate in energy between the valence band edge (VBE) and the conduction band edge (CBE), unlike typical semiconductors such as Si or GaAs (Figure 1a). The presence of an intermediate band allows the IBSCs to absorb three distinct, minimum-energy photons (equivalent to energies $h\nu_1$, $h\nu_2$, and $h\nu_3$ in Figure 1c), potentially yielding higher efficiencies than single-junction PVs. Theoretical estimates indicate that an optimal IBPV, with $E_g^{tot} \sim 2.0$ eV and subgaps E_g^1 and $E_g^2 \sim 1.2$ and 0.7 eV, respectively, potentially could achieve up to ~65% light-to-electricity conversion efficiency.¹³ Additionally, IBSCs potentially could be employed in applications such as light emitting diodes (LEDs) and lasers,⁵ which require radiative recombination of free carriers. IBSCs have yet to find commercial applications, however, primarily due to the lack of robust candidate materials possessing a partially filled, wide double-gap band structure. Hence, identification of promising candidates is an important step in realizing the practical utilization of highly efficient IBPVs.

Several nonconventional solar cell designs require additional materials that function as optically transparent yet conducting layers, typically referred to as transparent conducting oxides (TCOs), which can conduct free electrons (photoanodes) or free holes (photocathodes), thus facilitating transfer of photogenerated carriers into an external circuit. Notable examples are dye-sensitized solar cells (DSSCs)¹⁶ and polymer bulk-heterojunction cells,¹⁷ which rely on decoupling light absorption and charge-transport processes. Also, TCOs can improve the stability of high-efficiency perovskite semiconductors in single-junction devices.¹⁸ Typically, PVs utilize indium tin oxide as the TCO,¹⁹ with the cost and relative rarity of indium motivating the search for alternatives.²⁰ While n-type TiO₂ and ZnO have been studied extensively for photoanode applications,¹⁶ identification of optimal photocathodes is still an active area of research. Finding efficient p-type TCOs therefore is an important materials design challenge that will influence the development of novel solar cells, as well as the improvement of established technologies.

The discovery and optimization of materials, for the semiconductor(s) and other components used in a PV cell (e.g., a TCO), represents a significant challenge in the development of viable, beyond-Si technologies. Computational materials science, frequently using quantum mechanics (QM)-based methods to calculate properties of materials, has been

fairly successful in not only deepening our understanding of complex fundamental mechanisms in solid-state materials^{21,22} but also predicting candidates for various energy-related applications.^{23–30} In this feature article, we provide an overview of our own materials design and optimization research for novel solar cell applications. A detailed description of the types of QM calculations needed to evaluate various material properties, such as density functional theory (DFT),^{31,32} non-self-consistent GW (G_0W_0),^{33,34} unrestricted Hartree–Fock (UHF),³⁵ and complete active space self-consistent field (CASSCF)³⁶ calculations, is provided in the Supporting Information. The Supporting Information also details the benchmarking of theoretical predictions with available experimental data that is done before choosing a particular theoretical tool.

First-row transition-metal oxides (TMOs), which are composed of nonrare (hence inexpensive) elements that are potentially environmentally friendly to process, are promising candidates for beyond-Si PV. For example, NiO's intrinsic p-type nature and the charge-transfer (CT) character of its electronic structure make it an excellent candidate for both TCO and tandem DSSC applications. Additionally, the unique band structure of CoO makes it a contender for IBPVs while FeO could be a component of cheap solar energy conversion devices.^{37,38} Therefore, in section 2, we discuss the electronic structure of the pure oxides, namely, NiO (section 2.1),^{39,40} CoO (2.2),⁵ and FeO (2.3),⁴¹ identify their respective limitations, and devise strategies to engineer their corresponding band gaps via alloying/doping to improve optical properties. Also critical to PV applications is the separation of photogenerated carriers (electrons and holes) after light absorption and the efficient conduction of free carriers to external circuits to maximize electricity generated (section 3). We therefore discuss hole transport in NiO (section 3.1)^{40,42} and FeO (3.2)⁴³ and the potential to improve hole conduction via alloying and doping.

Apart from optical and charge transport properties, the bulk stability of a candidate material, specifically inhibiting the formation of any performance-limiting intrinsic defects, is important for both efficiency improvements and long-term life of a solar device (section 4). For example, bulk FeO is known to be unstable owing to the spontaneous formation of Fe vacancies.⁴⁴ Hence, section 4.1⁴⁵ explores alloying as a pathway to stabilize the rocksalt structure of FeO and suppress Fe-vacancy formation. In the case of Cu₂O (band gap ~2.2 eV), despite displaying promise as a candidate for thin-film PV, fabricated solar cells often exhibit poor efficiencies (~2%), which is attributed to the existence of intrinsic defects within

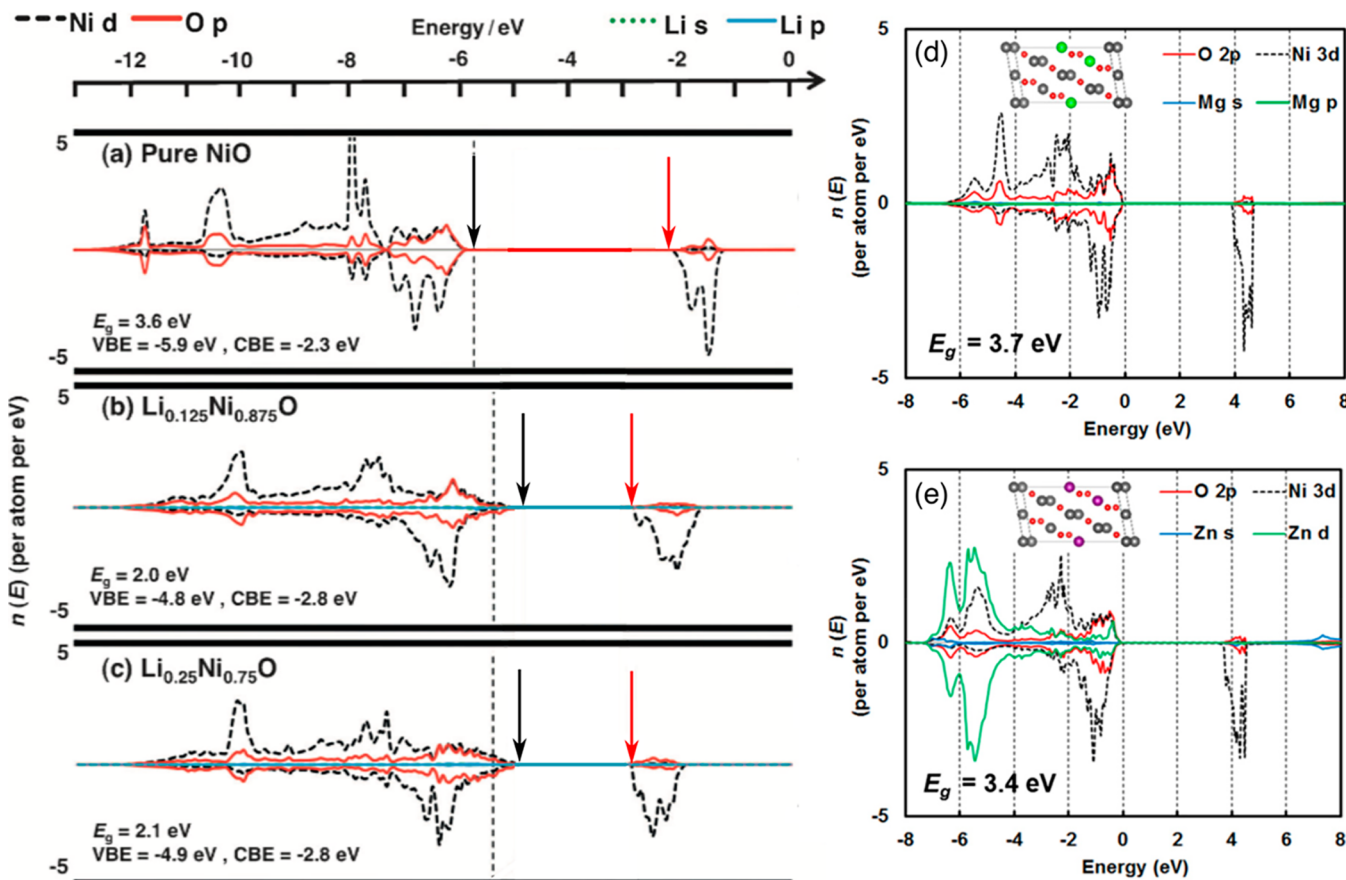


Figure 2. Projected density of states (PDOS) from PBE+ $U+\text{G}_0\text{W}_0$ in pure NiO (panel a), $\text{Li}_x\text{Ni}_{1-x}\text{O}$ (b and c), $\text{Mg}_x\text{Ni}_{1-x}\text{O}$ (d), and $\text{Zn}_x\text{Ni}_{1-x}\text{O}$ (e) alloys. Solid red and dashed black lines in all panels indicate respectively O p and Ni d states, while the green and blue lines correspond to states from the alloying element (Li, Mg, or Zn). The black and red arrows in panels a, b, and c indicate the valence and conduction band edges, respectively. Structure insets in panels d and e represent the SQS used. Positive (negative) PDOS refer to majority (minority) spin states. Panels a, b, and c adapted from ref 39. Copyright 2014 Wiley-VCH Verlag GmbH & Co. Panels d and e adapted from ref 40. Copyright 2015 American Institute of Physics.

Cu_2O that act as hole “traps”. Thus, section 4.2⁴⁷ is devoted to analyzing the role of intrinsic Cu vacancies in Cu_2O and potentially suppressing their formation via doping.

A notable semiconductor candidate for sustainable thin-film solar cells is the kesterite polymorph of $\text{Cu}_2\text{ZnSnS}_4$ (CZTS), which is made of abundant, nontoxic elements and exhibits an “ideal” single-junction gap (1.4–1.6 eV^{30,48}). However, PV devices based on CZTS have, so far, suffered from lower efficiencies (~12.6%) than crystalline Si or other thin-film cells (>20%). We therefore analyze the fundamental origins of poor crystal quality in kesterite CZTS, the role of antisites, and explore options (e.g., doping) for improving performance in section 4.3.^{50–53} Finally, we provide a summary of key ideas (section 5) to be employed for further exploration and calibration of materials in the design of highly efficient, beyond-Si solar cells. Section 6 offers brief concluding remarks.

2. BAND-GAP ENGINEERING VIA ALLOYING

2.1. NiO. Several solar energy conversion devices use NiO ,^{17,54,55} including PVs and DSSCs, due to several suitable intrinsic properties it possesses. For example, its large, indirect band gap (3.4–4.6 eV)⁵⁶ and p-type character due to intrinsic Ni vacancies⁵⁷ enable NiO to be a p-type TCO in PVs¹⁷ and in tandem DSSCs.⁵⁴ Although the CT character of its lowest-energy band excitation³⁹ should help ease electron–hole pair

separation,²⁴ its large, indirect band gap limits its application as a light absorber in solar cells. The band structure of NiO would need to be modified appropriately via suitable alloying, while preserving its favorable CT character, if NiO is to be employed as a light absorber. Given that prior studies have demonstrated good miscibility of Li_2O ,⁵⁸ MgO ,⁵⁹ and ZnO ⁶⁰ within the NiO lattice, Alidoust et al.^{39,40} explored the influence of these alloying partners on the band structure and transport properties of NiO .

Subsequent to using the Perdew–Burke–Ernzerhof (PBE⁶¹) density functional within DFT with a Hubbard U added on the transition metal ion (PBE+ U ^{62,63}) to accurately describe the ground-state electron exchange–correlation (XC), the authors^{39,40} performed G_0W_0 calculations (i.e., PBE+ $U+\text{G}_0\text{W}_0$; see the Supporting Information for details) to evaluate band gaps in alloyed NiO . This protocol of PBE+ $U+\text{G}_0\text{W}_0$ (with an *ab-initio*-derived $U_{\text{Ni}} = 3.8 \text{ eV}^{64}$) was used because it predicts a band gap for pure NiO (~3.6 eV,³⁹ Figure 2a) in agreement with experiments.⁵⁶ Furthermore, Alidoust et al. used special quasirandom structures (SQS)⁶⁵ to emulate homogeneous alloying⁶⁶ at $x = 0.25$ for $\text{Li}_x\text{Ni}_{1-x}\text{O}$,³⁹ $\text{Mg}_x\text{Ni}_{1-x}\text{O}$ and $\text{Zn}_x\text{Ni}_{1-x}\text{O}$,⁴⁰ while deriving the $\text{Li}_{0.125}\text{Ni}_{0.875}\text{O}$ structure from the SQS at $\text{Li}_{0.25}\text{Ni}_{0.75}\text{O}$.³⁹

The predicted projected density of states (PDOS) and band gaps in pure (panel a) and alloyed (panels b, c, d, and e) NiO

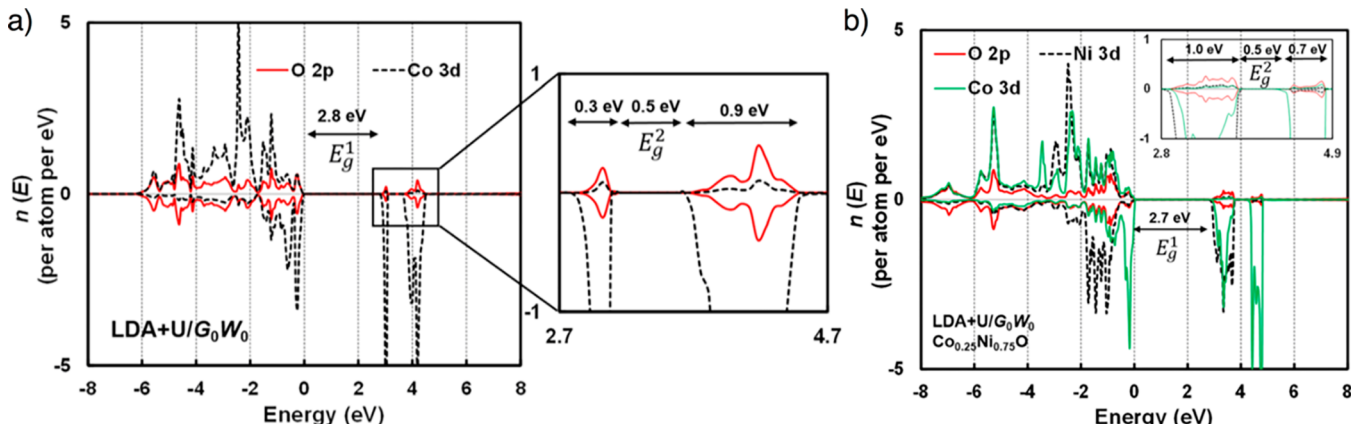


Figure 3. PDOS calculated using LDA+U+G₀W₀ on (a) CoO and (b) Co_{0.25}Ni_{0.75}O, respectively. The insets in both panels (horizontal axis) provide a closer look at the intermediate and conduction bands. Zero energies on both panels (horizontal axis) are set to the VBE. Positive (negative) PDOS refer to majority (minority) spin states. Adapted from ref 5. Copyright 2016 American Institute of Physics.

are plotted in Figure 2. Notably, the band gap in Li-alloyed NiO reduces from ~3.6 eV in pure NiO (Figure 2a) to ~2 eV at both Li_{0.125}Ni_{0.875}O (Figure 2b) and Li_{0.25}Ni_{0.75}O (Figure 2c). Thus, at high concentrations, the band gap is not sensitive to Li concentration in alloyed NiO, analogous to trends observed in other heavily doped semiconductors.⁶⁷ Importantly, adding Li introduces Li states at the VBE and broadens the observed peaks in the density of states (DOS), explaining the reduction in the band gap due to Li addition. Additionally, O 2p states are retained at the VBE in Li-alloyed NiO, signifying that the CT character of NiO is preserved, in agreement with prior absorption spectroscopy measurements.⁶⁸ However, Li_xNi_{1-x}O alloys still exhibit an indirect band gap, similar to pure NiO, which is beneficial for reducing carrier recombination but detrimentally affects light absorption. Nevertheless, alloying brings the band gap down to the visible range where most solar photons are, so that light absorption should increase significantly. This suggests that Li_{0.125}Ni_{0.875}O, for example, would be an excellent candidate, because of enhanced light absorption, to improve the efficiency of NiO-containing tandem DSSCs,⁶⁹ if used as a back electrode.

In the case of Mg_{0.25}Ni_{0.75}O (Figure 2d) and Zn_{0.25}Ni_{0.75}O (Figure 2e), the band gaps of the alloys, namely, 3.7 and 3.4 eV, respectively, are not significantly different from that of pure NiO (~3.6 eV, Figure 2a), signifying that both alloys should remain optically transparent. The lack of variation of the band gap in Mg_{0.25}Ni_{0.75}O can be attributed to the lack of Mg states at the band edges, which could arise from the larger band gap of MgO (~7.8 eV;⁷⁰ see discussion in section 2.3). Although Zn d states do exist at the VBE in Zn_{0.25}Ni_{0.75}O, the extent of hybridization is small due to their highly localized character, leading to insignificant influence on the gap. Importantly, both Mg and Zn alloys preserve the O 2p states at the VBE and the resultant CT character of NiO. Nevertheless, the optical transparency of Mg- and Zn-alloyed NiO, though not useful in the context of light absorption in PVs, is relevant for hole conduction when NiO is employed as a TCO (*vide infra*, section 3.1).

2.2. CoO. PV devices based on IBSCs require materials that possess an intrinsic band structure containing multiple valence/conduction bands with optimal energy gaps between them. TMOs, such as CoO with a band gap of 2.2–2.8 eV,⁷¹ are promising candidates for forming intermediate bands via

the crystal field splitting in d orbitals from neighboring O 2p orbitals. Thus, Alidoust et al.⁵ explored CoO and CoO–NiO alloys for potential IBSC applications. Specifically, the authors used the local density approximation (LDA)^{72,73} within DFT with *ab-initio*-derived Hubbard U parameters (LDA+U, U_{Co} = 4.0 eV approximated based on the value for Co³⁺,⁷⁴ and U_{Ni} = 3.8 eV³⁹) to describe electron XC in the ground state because analogous PBE+U calculations unphysically predict pure CoO to be a metal.⁵ Subsequently, Alidoust and co-workers⁵ employed LDA+U+G₀W₀ calculations to assess the band gap.

Figure 3a displays the PDOS of pure CoO, calculated using LDA+U+G₀W₀,⁵ with the inset focusing on the intermediate and conduction bands. The zero of the energy is set to the highest occupied level, i.e., the VBE. Notably, LDA+U+G₀W₀ predicts a double-gap structure, with individual gaps of ~2.8 and 0.5 eV, comparable to experiments⁷¹ and similar to qualitative predictions of LDA+U.⁵ However, the width of the intermediate band (between E_g¹ and E_g² in Figure 3a) is only 0.3 eV, which may inhibit light absorption and reduce the concentration of free carriers (electrons) in the intermediate band, eventually reducing efficiency. Additionally, the intermediate band in CoO is empty, and so no light absorption from the intermediate to the conduction band can occur, unless through multiphoton excitation, which probably would require solar concentrators to achieve.

To overcome the intrinsic limitations of CoO, and motivated by the strong CT character (which could increase carrier lifetimes at the intermediate band),^{24,64} the authors explored NiO as an alloying addition to CoO, with the hope of broadening the intermediate band and creating CT character at the band edges.⁵ A wide range of dopants considered to make the CoO–NiO alloy n-type (with the goal to partially occupy the intermediate band), e.g., Ga, In, Sc, Ti, V, Zr, Hf, and Nb, did not preserve the double-gap structure.⁵ The authors calculated the PDOS at various Ni concentrations ($x_{\text{Ni}} = 0.125, 0.25, 0.375, 0.5, 0.625, 0.75, \text{ and } 0.875$) in SQS and using LDA+U and LDA+U+G₀W₀. However, the double-gap band structure of CoO is preserved only at $x_{\text{Ni}} = 0.75$, i.e., at Co_{0.25}Ni_{0.75}O, among all the Ni concentrations considered (PDOS as displayed in Figure 3b).

At Co_{0.25}Ni_{0.75}O, the width of the intermediate band increases by ~0.7 eV compared to that of pure CoO, mitigating one of the limitations of pristine CoO. Also, the magnitude of E_g¹ varies marginally in Co_{0.25}Ni_{0.75}O (2.7 eV)

compared to that of pure CoO (2.8 eV, Figure 3a), while E_g^2 is identical in both oxides, suggesting a minor impact on the overall band gap properties with Ni addition. Interestingly, the VBE of $\text{Co}_{0.25}\text{Ni}_{0.75}\text{O}$ has a predominantly Co 3d character (instead of Ni 3d), similar to that of pure CoO (and unlike pure NiO), which indicates the lack of any CT character being imparted to the alloyed PDOS by NiO and a resultant negligible impact on carrier lifetimes. Nevertheless, metal-to-metal (i.e., Co d VBE to Ni d CBE) CT in $\text{Co}_{0.25}\text{Ni}_{0.75}\text{O}$ might yet contribute to improved carrier lifetimes via physical charge separation. The intermediate band has no partial occupation in the alloy either, and so its prospects for PV again may rely on use of concentrated solar fluxes. As noted by Alidoust et al.,⁵ the lack of partial filling of the intermediate band could prove to be useful for the inverse of solar PV, namely, LEDs and lasers, which rely on light emission from electronic excited states. Electrons at the CBE might decay radiatively at one color to the empty intermediate band and then undergo radiative recombination with holes at the VBE at another color, giving rise to multicolor LEDs or lasers. Both pure CoO and alloyed $\text{Co}_{0.25}\text{Ni}_{0.75}\text{O}$ thus are IBSCs worth further investigation for alternative PV, LED, and laser applications, as confirmed by rigorous LDA+U+G₀W₀ calculations.

2.3. FeO. FeO is an interesting candidate for solar applications,⁴¹ given its band gap in the visible region (~2.4 eV)^{75,76} and intrinsic nonstoichiometry (Fe cation vacancies) that enables cation transport needed in solar thermochemical materials.⁷⁷ However, practical FeO-based PV devices have to overcome several challenges, including the suboptimal band gap for light absorption (ideally ~1.5 eV) and the presence of Fe d character in both CBEs and VBEs, which could facilitate rapid radiative carrier recombination.⁷⁸ Hence, Toroker and Carter⁴¹ evaluated the impact of alloying on the electronic properties, specifically the band gap and the band edge character, using the Heyd–Scuseria–Ernzerhof (HSE) hybrid XC functional⁷⁹ in DFT DOS calculations. Ground-state DFT-HSE calculations, in the case of FeO,⁴¹ yield CBE-VBE eigenvalue gaps (~2.69 eV) in good agreement with experimental optical,⁷⁵ photoemission/inverse-photoemission (PES/IPES),⁸⁰ and theoretical G₀W₀ band gaps⁸¹ (~2.4 eV) and thus can be used reliably to predict actual band gaps. The authors employed SQS at $x = 0.25, 0.5$, and 0.75 in $\text{Fe}_{1-x}\text{M}_x\text{O}$ ($\text{M} = \text{Mg}, \text{Mn}, \text{Ni}, \text{or Zn}$), to estimate the band gap as a function of concentration, as plotted in Figure 4. The band gaps of the pure oxides ($x = 0$ and 1 in Figure 4), namely, FeO (~2.69 eV), MgO (~6.9 eV), MnO (~3.2 eV), NiO (~4.6 eV), and ZnO (~3.0 eV) are in qualitative agreement with experiment.⁴¹ In general, the band gaps of alloyed FeO follow the order $\text{Fe}_{1-x}\text{Mg}_x\text{O} > \text{Fe}_{1-x}\text{Mn}_x\text{O} > \text{Fe}_{1-x}\text{Ni}_x\text{O} > \text{Fe}_{1-x}\text{Zn}_x\text{O}$. Additionally, alloying FeO (between $x = 0.25$ and 0.75 in Figure 4) with Mn, Ni, or Zn leads to a reduction of the band gap, e.g., ~1.5 eV at $\text{Fe}_{0.5}\text{Zn}_{0.5}\text{O}$, which will be beneficial for PV applications.

Investigating the band edge character in FeO, Toroker and Carter⁴¹ found the VBE to exhibit predominantly Fe d character in both pure and alloyed FeO. In the case of $\text{Fe}_{1-x}\text{Mg}_x\text{O}$ and $\text{Fe}_{1-x}\text{Mn}_x\text{O}$ alloys, the Fe d character is present at the CBE also, similar to pure FeO, signifying a Mott–Hubbard insulating behavior. However, in $\text{Fe}_{1-x}\text{Ni}_x\text{O}$ and $\text{Fe}_{1-x}\text{Zn}_x\text{O}$, a significant number of Ni d-states and Zn s-states are present in the CBE, respectively, which will result in the production of holes (electrons) on the Fe (Ni/Zn) sites upon photon absorption, potentially reducing carrier recombi-

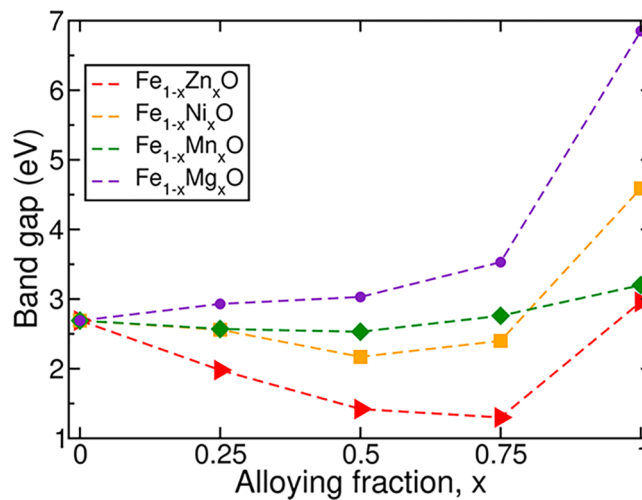


Figure 4. Band gap, calculated using DFT-HSE, as a function of the alloying concentration in FeO, alloying with Mg (purple circles), Mn (green diamonds), Ni (yellow squares), and Zn (red triangles). Adapted from ref 41. Copyright 2013 Royal Society of Chemistry.

nation. Additionally, the Zn s-states will be more delocalized⁸² than the Fe or Ni d-states at the CBE, improving transport (see section 3). Thus, Zn-alloyed FeO is an especially promising candidate for PV applications due to its predicted optimal band gap, expected low carrier-recombination rate, and expected improved carrier mobility. However, two potential flaws with FeO remain: its thermal metastability and intrinsic defects, namely, cation vacancies. Section 4 addresses these issues, suggesting that alloying may help with both, rendering the Zn-substituted FeO alloy worthy of further consideration.

We end this section with an intriguing design principle suggested by Toroker and Carter.⁴¹ They attributed the trends in band gaps and band edge character in alloyed FeO to the differences in band gap center (BGC) positions of the parent oxides. Note that the BGC is the average of the VBE and CBE, nominally corresponding to the Fermi level in an undoped insulator. Specifically, the alloys with large differences in BGC positions between the parent oxides (~1.4 eV between FeO and ZnO) compared to the corresponding differences in band gaps (~0.3 eV) exhibited smaller band gaps (e.g., ~1.3 eV for $\text{Fe}_{0.25}\text{Zn}_{0.75}\text{O}$, Figure 4). Additionally, when the difference in BGC position is large, insignificant hybridization occurs between the parent oxides at the band edges, leading to different types of electronic states dominating the VBEs (Fe d in $\text{Fe}_{1-x}\text{Zn}_x\text{O}$) and CBEs (Zn s), which can help with electron–hole pair separation. Notably, differences in BGC positions, unlike band edges, can be reliably obtained via simple DFT-based calculations⁸¹ or experimentally via work function measurements and can serve as a useful guide to identify promising alloying pairs.

3. OPTIMIZING CHARGE TRANSPORT VIA DOPING AND ALLOYING

3.1. NiO. Given the crucial role played by NiO as a hole conductor in TCOs,¹⁷ it is important to understand hole transport within NiO and identify potential limitations and strategies for improvement. Hole transport in NiO (and many transition metal oxides, including FeO;⁴³ see section 3.2) is activated and thus best described⁴² via the small polaron model^{83,84} (see the Supporting Information for details). In p-

doped samples such as the proposed Li-doped NiO light absorber discussed earlier, photoexcited minority carrier (electron) transport should not be rate-limiting, because the conduction band states are predicted to be highly delocalized and therefore not polaronic.⁶⁴ Thus, the study of hole transport in pure and doped NiO is sufficient to provide insight into its overall charge mobility. By using electrostatically embedded UHF and CASSCF calculations (see the Supporting Information), Alidoust and Carter^{40,42} estimated the diabatic (ΔG_{diab}^*) and adiabatic ($\Delta G_{\text{adiab}}^*$) barriers for hole migration in pure and Li-, Mg-, and Zn-doped NiO. All the predicted barriers are compiled in Table 1.^{40,42}

Table 1. Diabatic (ΔG_{diab}^*) and Adiabatic ($\Delta G_{\text{adiab}}^*$) Barriers for Hole Transport in Pure NiO and NiO Substitutionally Doped with Li, Mg, and Zn^{40,42a}

spin configuration	ΔG_{diab}^* (eV)	$\Delta G_{\text{adiab}}^*$ (eV)
Pure NiO		
i	0.36	0.10
ii	0.38	0.18
iii	0.40	0.11
Homogeneous $\text{Li}_{0.125}\text{Ni}_{0.875}\text{O}$		
$\text{Li}_1(\text{a})$	0.39	0.11
$\text{Li}_1(\text{b})$	0.38	0.20
$\text{Li}_2(\text{a})$	0.38	0.11
$\text{Li}_2(\text{b})$	0.40	0.13
$\text{Mg}_x\text{Ni}_{1-x}\text{O}$		
i	0.42	0.12
ii	0.42	0.19
iii	0.40	0.10
iv	0.37	0.11
v	0.37	0.11
vi	0.35	0.08
$\text{Zn}_x\text{Ni}_{1-x}\text{O}$		
i	0.46	0.14
ii	0.37	0.17
iii	0.34	0.08
iv	0.38	0.10
v	0.37	0.12
vi	0.38	0.10

^aSee text for description of the various spin configurations considered.

To estimate ΔG_{diab}^* in pure NiO, Alidoust and Carter⁴² considered electrostatically embedded NiO clusters of various sizes, namely $[\text{Ni}_2\text{O}_{10}]^{15-}$, $[\text{Ni}_{10}\text{O}_{28}]^{35-}$, and $[\text{Ni}_{28}\text{O}_{60}]^{63-}$, indicated in panels a, b, and c, respectively, of Figure 5. Three distinct spin configurations are possible for hole transport in bulk NiO (bottom panel of Figure 5) because of the anisotropic magnetic coupling between Ni cations in this material. For example, the Ni ions bridging the two oxygen atoms (labeled “1” and “2” in Figure 5) can be either ferromagnetically (FM) coupled (spin configurations i and ii) or antiferromagnetically (AFM) coupled (spin configuration iii). Additionally, the spin of the unpaired electron in the donor oxygen atom can be either parallel to the spin of the Ni 3d (e_g) states (configuration ii) or antiparallel (configuration i). Ni ions are FM-coupled within a given (111) plane and are AFM-coupled across adjacent (111) planes in rocksalt NiO.⁸⁵ Spin configurations i, ii, and iii therefore represent hole movement (a) through a (111) plane with Ni ions having opposite magnetic alignment to that of the unpaired electron on the donor oxygen; (b) away from the (111) plane and across a Ni

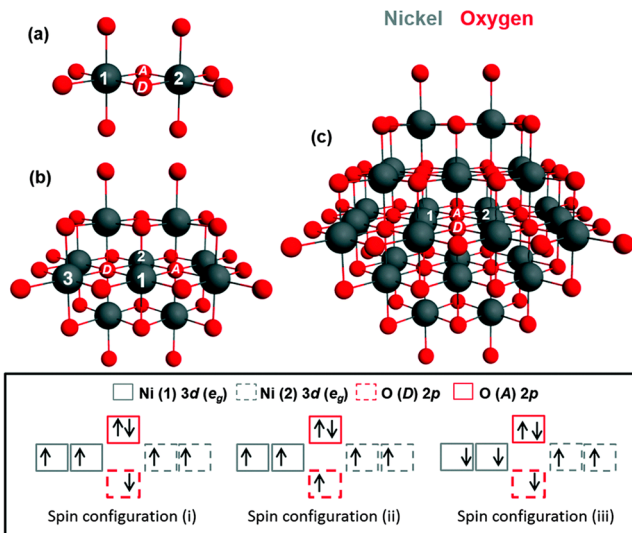


Figure 5. NiO clusters used for electrostatically embedded UHF and CASSCF calculations, namely, (a) $[\text{Ni}_2\text{O}_{10}]^{15-}$, (b) $[\text{Ni}_{10}\text{O}_{28}]^{35-}$, and (c) $[\text{Ni}_{28}\text{O}_{60}]^{63-}$. O (Ni) atoms are red (gray) spheres. Labels “D” and “A” on the oxygen atoms indicate hole donor and acceptor sites, while labels “1” and “2” indicate bridging Ni ions. The highlighted bottom panel shows the three distinct spin configurations considered for calculating hole transport barriers (see text). Adapted from ref 42. Copyright 2015 Royal Society of Chemistry.

plane that has the same magnetic alignment as the donor oxygen; and (c) parallel to a Ni (111) plane, respectively.

Interestingly, Alidoust and Carter⁴² found an insignificant difference in the diabatic barriers predicted by the various cluster sizes considered ($\Delta G_{\text{diab}}^* \sim 0.4\text{--}0.5$ eV) in pure NiO. Hence, the authors used the embedded $[\text{Ni}_{10}\text{O}_{28}]^{35-}$ as the parent cluster for subsequent diabatic barrier calculations. ΔG_{diab}^* for all spin configurations considered in pure NiO (0.36–0.40 eV, Table 1) are significantly higher than experimental estimates (0.09–0.14 eV^{86,87}), highlighting the importance of including adiabatic corrections to theoretically describe hole migration within NiO (see Figure S1 in the Supporting Information). The CASSCF calculations used to extract the coupling matrix elements defining the adiabatic corrections are significantly more computationally demanding than the UHF calculations sufficient for diabatic energies. Fortunately, CASSCF calculations on smaller embedded clusters, such as the $[\text{Ni}_2\text{O}_{10}]^{15-}$ (Figure 5a), are sufficient to reproduce the PES/IPES spectra of NiO,⁶⁴ suggesting both ground and excited states are well-described using this small embedded cluster. Alidoust and Carter⁴² therefore employed the embedded $[\text{Ni}_2\text{O}_{10}]^{15-}$ cluster (carved out of the $[\text{Ni}_{10}\text{O}_{28}]^{35-}$ cluster at the curve-crossing geometry) to obtain coupling matrix elements (V_{AB}) of 0.32, 0.22, and 0.32 eV for configurations i, ii, and iii, respectively.

Combining ΔG_{diab}^* from UHF (CASSCF energetics were similar) and V_{AB} from CASSCF, the authors⁴² evaluated $\Delta G_{\text{adiab}}^*$ in pure NiO as ~0.10, 0.18, and 0.11 eV for configurations i, ii, and iii, respectively (Table 1). Indeed, the addition of the adiabatic corrections results in better agreement between theory (0.10–0.18 eV) and experiment (0.09–0.14 eV^{86,87}). Interestingly, $\Delta G_{\text{adiab}}^*$ estimates highlight the anisotropy of hole transport within NiO, which is not apparent from ΔG_{diab}^* values (Table 1). For example, $\Delta G_{\text{adiab}}^*$ for hole migration away from a (111) plane (configuration ii, ~0.18 eV, Table 1) is nearly twice the barrier for hole

migration along a (111) plane (configuration iii, ~ 0.11 eV) or transfer through a (111) plane (configuration i, ~ 0.10 eV). The larger $\Delta G_{\text{adiab}}^*$ for configuration ii, compared to that of (i) and (iii), can be attributed to the destabilizing interatomic-exchange splitting experienced by the hole while migrating across a Ni (111) plane with opposite spins.⁴² Among configurations i and iii, the number of possible pathways with configuration iii in NiO is higher than for configuration i, signifying the higher impact of configuration iii on hole mobility. Hole transport within NiO therefore will be constrained to be parallel to (111) planes with the occasional transfer across (111) planes, as illustrated by the schematic in Figure 6a.

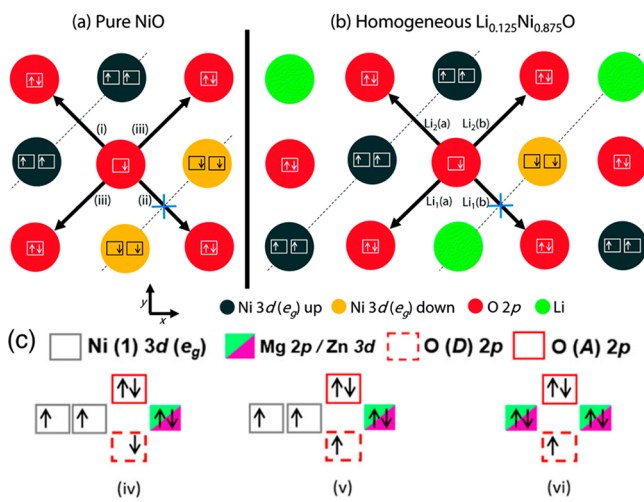


Figure 6. Hole migration in (a) pure NiO and (b) homogeneous $\text{Li}_{0.125}\text{Ni}_{0.875}\text{O}$ alloy. Red and green circles indicate O and Li atoms, respectively. Yellow and black circles correspond to Ni atoms with spins parallel and opposite to the unpaired donor oxygen. Dashed lines represent the (111) Ni planes, which are FM-coupled within the planes and AFM-coupled to each other. See text for description of the various Li configurations. Reproduced from ref 42. Copyright 2015 Royal Society of Chemistry. (c) Spin configurations iv, v, and vi considered in Mg- and Zn-doped NiO (see text for explanation). Adapted from ref 40. Copyright 2015 American Institute of Physics.

One strategy to potentially mitigate anisotropy of hole transport in NiO is to add dopants that might reduce exchange interactions between the migrating hole and the (111) cation planes, thereby facilitating isotropic hole transport. Li, an abundant element and a p-type dopant, is an obvious choice for doping, with prior experiments indicating that alloying NiO with Li preserves the rocksalt structure up to $x_{\text{Li}} = 0.25$.⁵⁸ Thus, Alidoust and Carter⁴² explored the effect of Li substitution on the hole-transport properties of NiO by considering electrostatically embedded clusters similar to $[\text{Ni}_{10}\text{O}_{28}]^{35-}$ (for UHF calculations) and $[\text{Ni}_2\text{O}_{10}]^{15-}$ (for CASSCF) used in pure NiO (Figure 5). The authors considered two distinct Li concentrations, namely, $[\text{Li}_1\text{Ni}_9\text{O}_{28}]^{36-}$ (indicated as “Li₁” in Table 1) and $[\text{Li}_2\text{Ni}_8\text{O}_{28}]^{37-}$ (“Li₂”), in order to model three local environments for hole movement: away from an O adjacent to a Li, between two O ions equidistant from a Li, and between two O ions that are each adjacent to different Li ions. There are two distinct spin configurations, (a) and (b), for each Li concentration, which are displayed schematically in Figure 6b. For example, Li₁(a) and Li₁(b) in the $[\text{LiNi}_9\text{O}_{28}]^{36-}$ cluster

refer to hole migration parallel to and away from a (111) plane, respectively, where Ni spins are parallel to the unpaired donor oxygen. Therefore, Li₁(a) and Li₁(b) are similar to spin configurations iii and ii, respectively, in pure NiO (Figure 5). Similarly, Li₂(a) and Li₂(b) in $[\text{Li}_2\text{Ni}_8\text{O}_{28}]^{37-}$ correspond to hole transfer through and parallel to a (111) plane, respectively, similar to configurations i and iii in Figure 5.

Interestingly, $\Delta G_{\text{adiab}}^*$ for removing a hole away from an oxygen atom adjacent to a Li⁺ in $[\text{LiNi}_9\text{O}_{28}]^{36-}$ is significantly higher (~ 1.3 eV,⁴² not shown in Table 1) than in pure NiO (~ 0.4 – 0.5 eV), suggesting that isolated Li⁺ ions act as hole traps in NiO. However, $\Delta G_{\text{adiab}}^*$ reduces dramatically (~ 0.4 – 0.5 eV, similar to pure NiO), for hole transfers between donor and acceptor oxygens that are adjacent and equidistant from a Li⁺. Thus, higher concentrations and better homogeneity of Li within NiO may be required for Li to be a useful dopant in NiO. However, $\Delta G_{\text{adiab}}^*$ for a homogeneous $\text{Li}_{0.125}\text{Ni}_{0.875}\text{O}$ alloy is similar to the diabatic barriers in pure NiO (~ 0.38 – 0.40 eV, Table 1).

To explore if adiabatic corrections to $\Delta G_{\text{adiab}}^*$ have a significant impact on hole migration in Li-doped NiO, Alidoust and Carter performed CASSCF calculations on embedded $[\text{LiNiO}_{10}]^{16-}$ clusters. Notably, V_{AB} along pathways $[\text{LiNiO}_{10}]_a^{16-}$ and $[\text{LiNiO}_{10}]_b^{16-}$, which are analogous to spin configurations i and ii in pure NiO with Li at a bridge site, are ~ 0.35 and 0.21 eV, respectively. Given the high computational expense of CASSCF calculations and the similarity of spin configurations in $[\text{Li}_2\text{Ni}_8\text{O}_{28}]_a^{37-}$ and $[\text{Li}_2\text{Ni}_8\text{O}_{28}]_b^{37-}$ to pathways i and iii in pure NiO, respectively, the authors assumed $V_{\text{AB}} = V_{\text{AB}}^{\text{NiO}}(i) \equiv V_{\text{AB}}^{\text{NiO}}(iii) = 0.32$ eV for the Li-doped case. Finally, combining the calculated $\Delta G_{\text{adiab}}^*$ and V_{AB} values yields $\Delta G_{\text{adiab}}^* \sim 0.11$, 0.20 , 0.11 , and 0.13 eV for configurations Li₁(a), Li₁(b), Li₂(a), and Li₂(b), respectively. Li doping therefore neither mitigates the anisotropy of the hole migration observed in pure NiO (Figure 6a), as suggested by the higher adiabatic barrier (~ 0.20 eV) for a hole to transfer away from a (111) plane versus along a (111) plane, nor improves the hole mobility via a reduction in $\Delta G_{\text{adiab}}^*$ (Table 1), consistent with experimental observations.⁸⁶ However, an increase in free hole concentration provided by homogeneous Li doping (rather than an increase in the mobility) may yet increase the overall hole conductivity in Li-doped NiO versus pure NiO.

Alidoust and Carter⁴⁰ subsequently explored Mg and Zn doping in NiO to see if introducing nonmagnetic M²⁺ ions could reduce the exchange coupling and hence the barrier along pathway (ii) mentioned earlier, thereby enabling three-dimensional (3-D) hole transport in NiO. MgO and ZnO should alloy with NiO readily, given that they both can form rocksalt oxides like NiO and have ionic radii similar to that of Ni²⁺ (~ 70 pm).⁸⁸ Being isovalent substituents to Ni²⁺, both Mg²⁺ and Zn²⁺ will not detrimentally trap holes, unlike Li⁺. The authors employed electrostatically embedded $[\text{MNi}_9\text{O}_{28}]^{35-}$ clusters (M = Mg/Zn) similar to $[\text{Ni}_{10}\text{O}_{28}]^{35-}$ (Figure 5b), and $[\text{MNiO}_{10}]^{11-}$ clusters analogous to $[\text{Ni}_2\text{O}_{10}]^{11-}$, to calculate $\Delta G_{\text{adiab}}^*$ and V_{AB} , respectively. In addition to the spin configurations i, ii, and iii that are encountered in pure NiO (Figure 5), three more spin configurations ((iv), (v), and (vi) in Figure 6c) are relevant for M-doped NiO. Specifically, pathways iv–vi correspond to hole transfer between oxygen sites with at least one nonmagnetic M²⁺ bridge site. Thus, configurations iv and v are similar to configurations i and ii, respectively, in pure NiO,

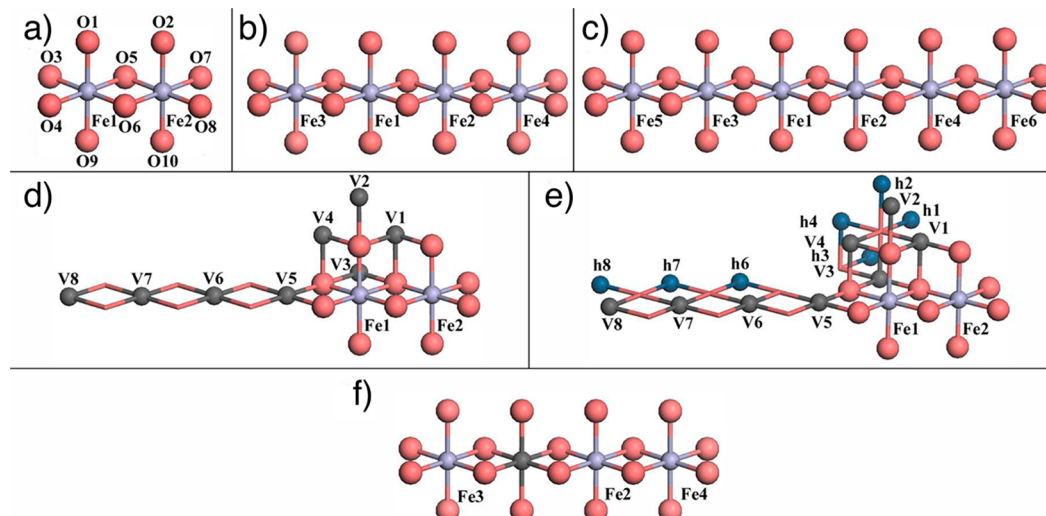


Figure 7. Representative structures of electrostatically embedded FeO clusters used in UHF calculations. Red, light blue, gray, and dark blue spheres indicate oxygen atoms, iron atoms, vacancies, and holes, respectively. Clusters (a) $[Fe_2O_{10}]^{15-}$, (b) $[Fe_4O_{18}]^{27-}$, and (c) $[Fe_6O_{24}]^{35-}$ have a single hole (not indicated here) without a cation vacancy. (d) $[Fe_2O_{10}]^{15-}$ corresponds to a cluster with both a single hole and a vacancy (in one of the V1–V8 sites). A vacancy in the V1–V5 sites reflects the removal of an ECP, while a vacancy in the V6–V8 sites corresponds to the removal of a 2+ point charge. (e) is the same cluster as (d) with an additional hole (denoted by h1–h8), resulting from replacing a 2+ point charge with a 3+ point charge. (f) is $[Fe_3O_{18}]^{28-}$ with one Fe vacancy with the resultant holes on the Fe2 and Fe3 sites. Adapted from ref 43. Copyright 2012 American Chemical Society.

with one of the bridge Ni^{2+} sites being replaced by a M^{2+} . Configuration vi corresponds to both of the bridge sites being occupied by a nonmagnetic M^{2+} and represents high levels of M doping.

For the migration of a hole from a donor site adjacent to a M^{2+} ion (site “3” in Figure 5b) with both bridge sites being Ni^{2+} (configurations i–iii), both $\Delta G_{\text{adiab}}^*$ and $\Delta G_{\text{adiab}}^{*}$ exhibit trends similar to that of pure NiO. For example, Mg- (Zn-)doped NiO exhibits $\Delta G_{\text{adiab}}^* \sim 0.12$ (0.14), 0.19 (0.17), and 0.10 (0.08) eV for configurations i, ii, and iii, respectively (Table 1). Note that both Mg- and Zn-doped NiO display a higher barrier for the hole to move either through or away from a (111) plane (0.19 and 0.17 eV), exhibiting anisotropy similar to that of pure NiO. Thus, if Mg or Zn atoms are away from the bridge site, alloyed NiO exhibits a barrier and anisotropy similar to pure NiO.

Interestingly, the extent of anisotropy on hole migration in alloyed NiO is significantly reduced if Mg or Zn occupies a bridge site. For example, $\Delta G_{\text{adiab}}^*$ for hole migration through, away from, and parallel to a (111) plane, are ~ 0.11 , 0.11, and 0.08 eV, respectively (Table 1), in the Mg-doped sample, while the corresponding barriers in the Zn-doped NiO are ~ 0.10 , 0.12, and 0.10 eV, respectively. Thus, both Mg and Zn bridge sites significantly reduce the barrier for hole movement away from the (111) plane, reducing anisotropy. Furthermore, the magnitude of the migration barrier for configurations iv–vi in Mg- and Zn-doped samples (~ 0.1 eV) is comparable to the lowest barriers found in pure NiO, indicating that both Mg and Zn mitigate anisotropy while preserving the fast hole conduction channels in NiO. Note that the impact of the calculated hole migration barriers on the macroscopic hole conduction will depend on both the concentration and homogeneity (i.e., total number of available facile conduction channels) of Mg/Zn within NiO. Hence, Mg and Zn doping signifies a promising pathway forward to improve 3-D hole transport in NiO for solar applications, making NiO a more

efficient TCO, unlike homogeneous Li alloying that does not mitigate the intrinsic two-dimensional transport in NiO.

3.2. FeO. Apart from the intrinsic electronic properties of FeO (section 2.3), another important challenge for FeO-based solar devices is the low hole mobility, commonly attributed to lattice distortions in the presence of a hole.⁸⁹ Prior experimental studies reported improved hole conduction in FeO⁹⁰ via increasing the concentration of Fe vacancies (V_{Fe}) and introducing p-type dopants (e.g., Cu⁺).⁹¹ Thus, Toroker and Carter⁴³ explored the impact of V_{Fe} , p-dopants (Cu⁺, Li⁺, and Na⁺), and n-dopants (interstitial H⁺) on the diabatic hole migration barrier ($\Delta G_{\text{adiab}}^*$) using UHF calculations on electrostatically embedded clusters (similar to section 3.1; see more details in the Supporting Information). Unlike NiO, the adiabatic correction to the hole migration barrier in FeO is insignificant (~ 0.01 eV). All Fe cations are in a FM spin ordering in the cluster models, because of the higher activation energy for hole transfer across AFM planes of Fe,⁴³ similar to hole transport in NiO (Figure 6a). Unlike NiO, hole transfer is between the metal cations, not the oxygen anions.

Figure 7 shows the representative structures of electrostatically embedded FeO clusters that were used by Toroker and Carter⁴³ during the UHF calculations. Red, light blue, gray, and dark blue spheres indicate oxygen atoms, Fe atoms, vacancies, and holes, respectively. The authors observed that the two holes created by an iron vacancy in (pure and doped) FeO localize on two Fe cations, on the basis of the Fe d character of the VBE and a Bader analysis of the charge distribution. Four distinct cluster models of pure FeO were considered, namely: (i) Model 1, a negatively charged $[Fe_2O_{10}]^{15-}$ cluster (Figure 7d) with only one hole, containing two Fe cations and one Fe vacancy, modeled by removing either an effective core potential (ECP, V1–V5 sites) or a 2+ point charge (V6–V8); (ii) Model 2, a neutral $[Fe_2O_{10}]^{14-}$ with two holes (Figure 7e), where the second hole is added at a distant point charge site; (iii) Model 3, a larger, negatively charged $[Fe_3O_{18}]^{28-}$ (Figure 7f), with a single V_{Fe} introduced

by removing an Fe site and containing only one hole; and (iv) Model 4, a neutral $[\text{Fe}_3\text{O}_{18}]^{28-}$ cluster, with holes localized on the Fe2 and Fe3 sites. The authors evaluated hole migration between the Fe1 and Fe2 sites in Models 1 and 2 and in between the Fe2 and Fe4 sites in Models 3 and 4, in order to understand the effect of V_{Fe} and spectator holes on hole migration.

For generating clusters to represent Cu-, Li-, and Na-doped FeO, one of the Fe sites is replaced by the dopant in $[\text{Fe}_2\text{O}_{10}]^{15-}$, resulting in a formal charge of -16 (Figure 7a) and the Fe4 site is substituted by the dopant in $[\text{Fe}_4\text{O}_{18}]^{27-}$ (formal charge of -28 , Figure 7b). In the case of the n-type interstitial H^+ , the donated electron may recombine with one of the naturally occurring holes in FeO (due to intrinsic Fe vacancies), resulting in three distinct models: (i) $[\text{Fe}_2\text{HO}_{10}]^{14-}$ where the H^+ is bonded to O5 in Figure 7a and is located between O5 and O6 with the hole transferring between Fe atoms adjacent to H^+ ; (ii) $[\text{Fe}_4\text{HO}_{18}]^{26-}$ with hole transfer away from a Fe atom, i.e., Fe1 in Figure 7b, adjacent to H^+ ; and (iii) $[\text{Fe}_3\text{HO}_{18}]^{28-}$ (similar to Model ii, which considers the presence of H^+ alongside an Fe vacancy during hole migration).

Table 2 compiles the calculated activation energy (ΔG^*) and the free energy change (ΔG), for the various cluster

Table 2. Diabatic Activation Barriers (ΔG^*) and Free Energy Change (ΔG) for Hole Migration from a Donor Atom (D) to an Acceptor (A) atom (D → A, or Vice Versa) in Pure, p-, and n-Doped FeO^{43 a}

cluster	activation energy, ΔG^* (eV)		free energy, ΔG (eV)
	D → A	A → D	
Pure FeO			
${}^{\text{@}}[\text{Fe}_2\text{O}_{10}]^{15-}$	0.53		0
$[\text{Fe}_2\text{O}_{10}]^{15-}$ (V1)	0.55		0
${}^{\#}[\text{Fe}_2\text{O}_{10}]^{15-}$	1.51–0.69	0.42–0.11	1.4–0.27
$[\text{Fe}_3\text{O}_{18}]^{29-}$	1.44	0.13	1.31
$[\text{Fe}_3\text{O}_{18}]^{28-}$	1.05	0.23	0.82
p-Doped FeO			
$[\text{FeCuO}_{10}]^{16-}$	0.1	1.59	−1.50
$[\text{Fe}_3\text{CuO}_{18}]^{28-}$	0.20	0.98	−0.78
$[\text{FeLiO}_{10}]^{16-}$	2.34	0.07	2.27
$[\text{Fe}_3\text{LiO}_{18}]^{28-}$	0.19	1.00	−0.81
$[\text{FeNaO}_{10}]^{16-}$	2.58	0.10	2.48
$[\text{Fe}_3\text{NaO}_{18}]^{28-}$	0.26	0.90	−0.64
n-Doped FeO			
$[\text{Fe}_2\text{HO}_{10}]^{14-}$	0.67		0
$[\text{Fe}_4\text{HO}_{18}]^{26-}$	0.20	1.02	−0.83
$[\text{Fe}_3\text{HO}_{18}]^{28-}$	0.79	0.35	0.44

^aSee text for explanations of the various clusters used. ${}^{\text{@}}[\text{Fe}_2\text{O}_{10}]^{15-}$: cluster with a single hole and no cation vacancies (Figure 7a).

${}^{\#}[\text{Fe}_2\text{O}_{10}]^{15-}$: cluster with a single hole and a cation vacancy (model 1 in text, Figure 7d).

configurations considered by Toroker and Carter⁴³ in pure, p-, and n-doped FeO. D → A (A → D) indicates the hole migration from the donor (acceptor) to the acceptor (donor) site, and the free energy change is negative if the acceptor state is lower in energy than the donor. The range of activation energies indicated for ${}^{\#}[\text{Fe}_2\text{O}_{10}]^{15-}$ signifies the various vacancy configurations (V2–V8, Figure 7d), while $[\text{Fe}_2\text{O}_{10}]^{15-}$ (V1) corresponds to the V1 configuration in Figure 7d.

The activation energy for isolated hole migration in pristine FeO (${}^{\text{@}}[\text{Fe}_2\text{O}_{10}]^{15-}$ in Table 2, Figure 7a) is predicted to be ~ 0.53 eV, much higher than values measured in FeO containing 5% Fe vacancies (~ 0.16 eV);⁹¹ the overestimation was attributed to the overestimation of bond lengths by UHF in FeO.⁴³ Interestingly, introduction of a cation vacancy located symmetrically between the donor and acceptor Fe sites (V1 in Figure 7d) does not affect the activation energy for isolated hole migration (~ 0.55 eV), in qualitative agreement with an observed insensitivity of hole activation barriers to V_{Fe} concentration.⁹¹ However, V_{Fe} located asymmetrically with respect to the donor and acceptor sites (V2–V8 in Figure 7d) breaks the symmetry between the two states, resulting in free energy changes of ~ 0.3 – 1.4 eV (Table 2) while also causing significant increases in hole migration barriers ($D \rightarrow A \sim 0.69$ – 1.51 eV, Table 2). Intrinsic V_{Fe} therefore can act as trap sites for hole migration away from V_{Fe} . Interestingly, the presence of a second hole along with V_{Fe} near the donor site reduces the barrier for hole transport away from the donor site, presumably due to the electrostatic repulsion between the two holes. For example, the activation barrier (and free energy change) decreases from ~ 1.4 eV (~ 1.31 eV) in $[\text{Fe}_3\text{O}_{18}]^{29-}$ with a single hole (Figure 7f) to ~ 1.05 eV (~ 0.82 eV) in $[\text{Fe}_3\text{O}_{18}]^{28-}$ with two holes (Table 2). Hence, excess holes may aid hole transport in undoped FeO, beyond just increasing the conductivity via their increased concentration. Overall, though, hole transport in FeO is predicted to mostly occur among Fe cations either not near or residing equivalently across an Fe vacancy.

In the case of p-doped FeO, Cu ions are predicted to act as trap sites for holes, while Li and Na ions force hole localization on Fe. For example, the free energy change for hole transfer from Fe to Cu is ~ -1.50 eV ($[\text{FeCuO}_{10}]^{16-}$, Table 2), while holes in Li- and Na-doped FeO ($[\text{FeLiO}_{10}]^{16-}$ and $[\text{FeNaO}_{10}]^{16-}$, Table 2) are transferred to a nearby oxygen ion instead of either Li or Na cations. However, the large, positive free energy change for hole transfer to an adjacent oxygen ion in $[\text{FeLiO}_{10}]^{16-}$ and $[\text{FeNaO}_{10}]^{16-}$ (~ 2.27 – 2.48 eV, Table 2) indicates that a hole in Li- and Na-doped FeO is likely to remain localized on an Fe ion. The lack of hole transfer to either Li^+ or Na^+ is due to the large second ionization potential (IP) of both elements; transfer of a hole effectively ionizes a core electron in these cases, which is very unfavorable, whereas for Cu^+ only a valence electron is ionized, which is less costly. All p-dopants in FeO tend to favor hole transfer toward Fe ions adjacent to the dopant, as indicated by ΔG of ~ -0.78 , -0.81 , and -0.64 eV in Cu-, Li-, and Na-doped FeO, respectively (Table 2, Figure 7b with Fe4 substituted by the dopant). The tendency to attract holes to Fe cations near p-dopants lowers electrostatic repulsion of the hole via the lower charge state of the dopant ion compared to that of an Fe cation.

Interestingly, H does not act as a hole trap for n-doped FeO, in contrast to findings in an analogous system, namely, n-doped Li_2O .⁹² For example, ΔG^* (ΔG) for a hole transfer in the presence of a H and V_{Fe} (i.e., the $[\text{Fe}_3\text{HO}_{18}]^{28-}$ cluster, Table 2) is ~ 0.79 eV (~ 0.44 eV), which is lower than ~ 1.44 eV (~ 1.31 eV) in undoped FeO ($[\text{Fe}_3\text{O}_{18}]^{29-}$). H actually drives holes away from its site, illustrated by the negative ΔG (~ -0.83 eV, Table 2) for hole migration away from an Fe ion adjacent to H (in $[\text{Fe}_4\text{HO}_{18}]^{26-}$). This tendency of H is due to the strength of the O–H bond, as the presence of a nearby hole will dramatically weaken the O–H bond. However, H

increases the barrier for hole migration marginally (~ 0.67 eV) compared to that of undoped FeO (~ 0.53 eV) when symmetrically located across the Fe sites (in $[\text{Fe}_2\text{HO}_{10}]^{14-}$ in Table 2). Since the recombination of the excess electron donated by H, with an existing hole created by the intrinsic Fe vacancies in FeO is assumed during the UHF calculations, H doping can beneficially improve the hole transport in FeO as long as the excess electrons from H are neutralized by the intrinsic holes.

4. BULK STABILITY AND DEFECTS

4.1. Stabilizing Bulk Rocksalt-FeO. The thermodynamic instability of bulk rocksalt FeO, which spontaneously forms $\sim 5\%$ Fe vacancies⁴⁴ and is only thermodynamically stable at elevated temperatures, is an important performance-limiting criterion in FeO-based solar devices. One strategy to stabilize bulk FeO is to alloy with other suitable oxides, e.g., MgO, MnO, NiO, and ZnO. Hence, using a generalized gradient approximation (GGA)⁶¹ XC functional with a U added (i.e., GGA+ U), Toroker and Carter⁴⁵ evaluated the formation energy of V_{Fe} in pure and alloyed FeO. The specific values of U used by the authors⁴⁵ were 3.7, 3.5, and 3.8 eV for Fe^{2+} ⁹³, Mn^{2+} ⁹⁴, and Ni^{2+} ³⁹, respectively. To calculate the vacancy formation energies, the authors chose O-rich conditions (μ_{Fe} set by the $\text{FeO}-\text{Fe}_2\text{O}_3$ equilibrium) to avoid mixing GGA (accurate for Fe metal) and GGA+ U (Fe-oxides) energies.⁴⁵ Also, the authors added zero-point energies (ZPEs) and thermal corrections due to phonons (calculated using the PHONOPY software⁹⁵) to the GGA+ U -calculated total energies. Furthermore, SQS^{65,96} were employed to model homogeneously alloyed FeO at $\text{Fe}_{0.5}\text{M}_{0.5}\text{O}$ ($\text{M} = \text{Mg}, \text{Mn}, \text{Ni}$, and Zn).

Figure 8 plots the V_{Fe} formation energy in pure FeO and $\text{Fe}_{0.5}\text{M}_{0.5}\text{O}$ under oxygen-rich conditions, where blue, black, and yellow squares denote GGA+ U total energies, GGA+ U total energies corrected with ZPEs (i.e., free energy at 0 K), and GGA+ U total energies corrected with ZPEs and thermal corrections up to 300 K (i.e., free energy at 300 K),

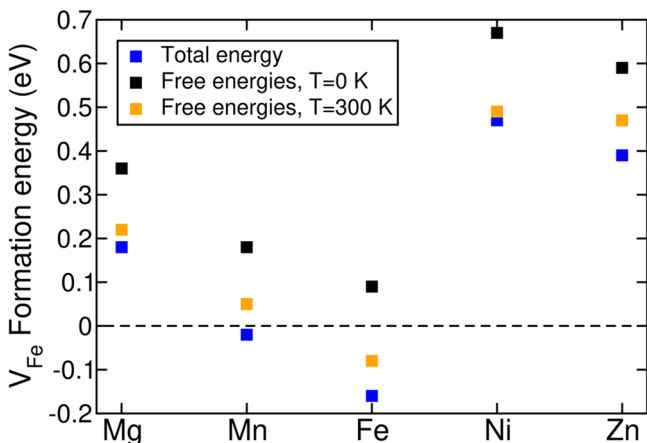


Figure 8. Iron vacancy (V_{Fe}) formation energies under oxygen-rich conditions in pure and alloyed FeO. Note that each alloying element (M) corresponds to a $\text{Fe}_{0.5}\text{M}_{0.5}\text{O}$ composition (i.e., Mg corresponds to $\text{Fe}_{0.5}\text{Mg}_{0.5}\text{O}$). Blue, black, and yellow squares represent the formation energies calculated using GGA+ U total energies, free energies at 0 K (i.e., total energy + ZPE), and free energies at 300 K (total energy + ZPE + thermal correction due to phonons), respectively. Adapted from ref 45. Copyright 2015 Springer US.

respectively. Note that the addition of ZPEs and/or thermal corrections changes the vacancy formation energy negligibly (~ 0.1 eV, Figure 8). The negative V_{Fe} formation energy (~ -0.1 eV) in pure FeO is consistent with the experimentally observed off-stoichiometry of FeO.⁴⁴ On the basis of both the lower bound (total energies, blue squares in Figure 8) and the average values of V_{Fe} formation energies, it can be concluded that alloying FeO with Mg, Mn, Ni, or Zn does suppress V_{Fe} formation significantly. Notably, the increase in calculated V_{Fe} formation energy with Mn alloying is consistent with experimental observations of a decreased V_{Fe} concentration with Mn addition.⁹⁷ Ni and Zn cause the highest increase in the V_{Fe} formation energy, indicating that alloying with Ni and Zn might be most effective in stabilizing the FeO bulk structure.

4.2. Point Defects and Doping in Cu₂O. Cu₂O is a promising candidate for low-cost and sustainable solar applications, exhibiting an optical band gap (~ 2.17 eV)⁹⁸ within the visible solar spectrum. However, Cu₂O-based heterojunction solar cells thus far have achieved only low efficiencies ($\sim 2\%$),⁴⁶ which have been attributed to rapid carrier recombination in bulk Cu₂O and intrinsic defects that inhibit minority carrier diffusion and photoconductivity. Cu₂O is a p-type semiconductor due to the presence of Cu vacancies.⁵⁹ It therefore is important to understand how intrinsic defects in Cu₂O act as trap sites and devise strategies, e.g., isovalent and aliovalent doping in Cu₂O, to improve minority carrier conduction. We review the computational work by Isseroff and Carter⁴⁷ on the aforementioned topics in this section.

Two types of intrinsic Cu vacancies can exist:⁴⁷ (i) a simple Cu vacancy (V_{Cu}), where a vacancy substitutes a 2-fold coordinated Cu site (orange sphere in Figure 9a) and (ii) a split Cu vacancy ($V_{\text{Cu}}^{\text{split}}$), where a vacant Cu site allows a nearby Cu atom to move into a tetrahedrally coordinated site (cyan sphere in Figure 9b). Theoretical studies prior to Isseroff and

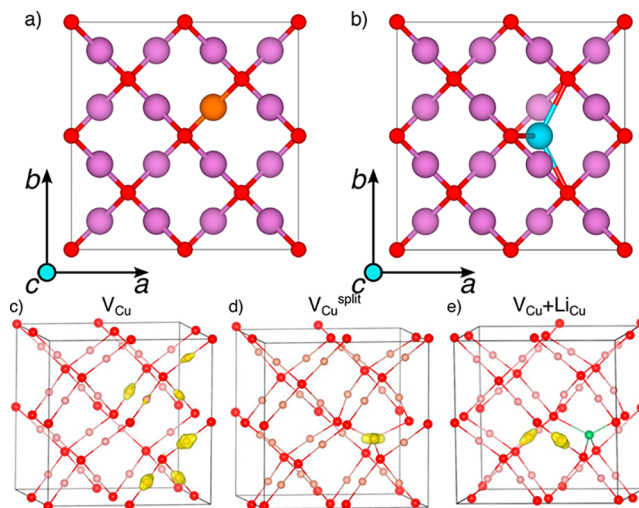


Figure 9. Illustration of (a) a simple Cu vacancy (V_{Cu} , orange sphere) and (b) a split Cu vacancy ($V_{\text{Cu}}^{\text{split}}$, cyan sphere). Excess spin density with (c) V_{Cu} , (d) $V_{\text{Cu}}^{\text{split}}$ in pure Cu₂O, and (e) a V_{Cu} in Li-doped Cu₂O. Red and pink (or purple) spheres in all panels represent O and Cu, respectively. The green sphere in (e) corresponds to Li. The isosurface level in each panel is set to half of the maximum density, at (a) 0.014, (b) 0.070, and (c) 0.032 e Å⁻³, respectively. Panels c–e are adapted from ref 47. Copyright 2013 American Chemical Society.

Carter,^{100–103} using a variety of XC functionals within DFT, were inconsistent in their predictions of Cu vacancy formation energies and the existence of hole traps in Cu_2O , prompting the authors⁴⁷ to use a combination of GGA+U ($U = 6$ eV)¹⁰⁴ and DFT-HSE calculations with denser k -point grids to resolve the discrepancies in DFT-based predictions. To evaluate vacancy formation energies, the authors considered two distinct chemical scenarios that could avoid precipitation of metallic Cu: (i) Cu-rich/O-poor (Cu_2O in equilibrium with CuO) and (ii) Cu-poor/O-rich (Cu_2O in equilibrium with oxygen gas).

Panels c and d of Figure 9 plot the excess spin density, obtained using HSE calculations, in pure Cu_2O with a V_{Cu} (panel c) and a $V_{\text{Cu}}^{\text{split}}$ (panel d), where the red and pink atoms correspond to O and Cu. The isosurface in both panels is set to half of the maximum density, specifically at 0.014 and 0.070 $e \text{Å}^{-3}$ for V_{Cu} and $V_{\text{Cu}}^{\text{split}}$, respectively. Figure 9c exhibits significant hole delocalization across several neighboring Cu atoms in Cu_2O upon V_{Cu} formation. However, the hole density is localized on one Cu atom near the $V_{\text{Cu}}^{\text{split}}$ (Figure 9d), signifying that $V_{\text{Cu}}^{\text{split}}$ can act as a hole trap. Additionally, HSE-DOS calculations by the authors⁴⁷ displayed significant DOS close to the Fermi level with V_{Cu} and a distinct acceptor state at 0.57 eV well above the Fermi level with $V_{\text{Cu}}^{\text{split}}$. This is in qualitative agreement with experimental ionization levels,¹⁰⁵ signifying that $V_{\text{Cu}}^{\text{split}}$ is indeed a hole trap.

Isseroff and Carter⁴⁷ reported lower formation energies for V_{Cu} than for $V_{\text{Cu}}^{\text{split}}$ across DFT XC functionals, including PBE (V_{Cu} more stable than $V_{\text{Cu}}^{\text{split}}$ by ~0.18 eV), PBE+U (by ~0.17 eV), and HSE (by ~0.24 eV), under both Cu-rich and Cu-poor conditions. However, the absolute formation energies of V_{Cu} (~0.66 eV) and $V_{\text{Cu}}^{\text{split}}$ (~0.84 eV) both fall within experimental estimates (0.39–0.97 eV^{47,106,107}) only when using PBE+U and under Cu-poor conditions, indicating the sensitivity of vacancy formation energies in Cu_2O to experimental conditions. HSE (PBE) overestimates (underestimates) V_{Cu} and $V_{\text{Cu}}^{\text{split}}$ formation energies compared to PBE+U's estimates, under both Cu-rich and Cu-poor conditions.⁴⁷ Nevertheless, the agreement between the different levels of XC functionals on the relative stability of V_{Cu} and $V_{\text{Cu}}^{\text{split}}$, unlike previous theoretical work,^{100–103} gives credibility to the theoretical methods employed in ref 47 and establishes V_{Cu} to be the dominant defect in pure Cu_2O . However, the small energy difference (0.17–0.24 eV) between V_{Cu} and $V_{\text{Cu}}^{\text{split}}$ signifies that both defects can coexist at room temperature, particularly if the defects are “frozen-in” after high-temperature annealing treatments.¹⁰⁸ It therefore is important to devise strategies, such as doping the Cu_2O lattice, to suppress formation of hole traps, i.e., $V_{\text{Cu}}^{\text{split}}$. Specifically, dopants such as Li, Mg, Mn, and Zn, which possess either a stable closed-shell or half-filled shell configuration²⁴ and have ionic radii similar to that of Cu^+ ,⁸⁸ are promising candidates since they should be less likely to form trap sites in Cu_2O .

Table 3 lists the formation energy of V_{Cu} in both pure and doped Cu_2O , as calculated via DFT-HSE, for both Cu-rich and Cu-poor conditions. For all n-type dopants considered, namely, Mg^{2+} , Mn^{2+} , and Zn^{2+} , the V_{Cu} formation energy decreases considerably (by ~1–2 eV, Table 3) in comparison to that of pure Cu_2O (~1.337–1.152 eV), suggesting a substantial increase in V_{Cu} concentration for n-doped Cu_2O . The lowering of the vacancy formation energy due to n-dopants can be attributed largely to the charge compensation between the excess electron introduced by the dopant and the

Table 3. Formation Energy for a Simple Cu Vacancy (V_{Cu}) in Pure and Doped Cu_2O , Calculated Using DFT-HSE^{47a}

composition	V_{Cu} formation energy (eV)	
	Cu-rich/O-poor	Cu-poor/O-rich
pure Cu_2O	1.337	1.152
doped Cu_2O		
Li	1.102	0.918
Mg	−2.228	−2.412
Mn	−1.341	−1.526
Zn	−1.389	−1.573

^aCu-rich and Cu-poor conditions correspond to Cu_2O in equilibrium with CuO and O_2 gas, respectively.

excess hole introduced by the vacancy, in agreement with reported experimental difficulties obtaining n-type Cu_2O .¹⁰⁹

Surprisingly, isovalent doping of Cu_2O , using Li^+ , also leads to a reduction in the vacancy formation energy by ~0.2 eV (Table 3), suggesting that structural changes could be significant in doped- Cu_2O . Note that all dopants considered have a minimum coordination of four (i.e., tetrahedral) for most compounds in which they naturally occur,¹¹⁰ whereas Cu is 2-fold coordinated in Cu_2O . While the dopant is forced to conform to the 2-fold Cu coordination in pristine Cu_2O , a nearby Cu vacancy allows the dopant to move to an intermediate position (analogous to the Cu movement in $V_{\text{Cu}}^{\text{split}}$, Figure 9b) where they can adopt a tetrahedral coordination with the neighboring oxygen atoms. Thus, the ability of the dopant atom to find a preferred tetrahedral coordination contributes significantly to stabilization of V_{Cu} by both n-type and isovalent dopants. A positive consequence of dopants preferring a tetrahedral coordination is destabilization of the $V_{\text{Cu}}^{\text{split}}$ trap site, since formation of $V_{\text{Cu}}^{\text{split}}$ requires a Cu atom to be present in the intermediate 4-fold coordinated site instead of the dopant. Hence, addition of (isovalent and n-type) dopants in Cu_2O may improve hole migration via destabilization of $V_{\text{Cu}}^{\text{split}}$ trap sites.

Additionally, the electronic isosurface in Li-doped Cu_2O (Figure 9e, green sphere is Li) indicates a marginal hole localization on two of the next-nearest-neighbor (NNN) Cu atoms from the Li, unlike V_{Cu} in pure Cu_2O . However, HSE-DOS calculations in Li-doped (and n-doped) Cu_2O did not indicate the presence of any distinct single-particle states within the gap,⁴⁷ signifying the lack of hole traps. Also, Isseroff and Carter found a negligible driving force (<0.1 eV) for Cu vacancies to cluster adjacently to n-dopants, indicating that n-dopants should impact hole conductivity only marginally unless they are present at high concentrations.⁴⁷ Thus, these dopants, especially Li because it will not reduce the number of free carriers via charge compensation, warrant further tests to see if doping can improve photoconductivity of Cu_2O .

4.3. Antisites in CZTS. CZTS displays promise for beyond-Si thin-film PV devices because of its optimal-energy, direct band gap (1.4–1.6 eV⁴⁸) and because it is made of abundant, nontoxic constituents that can be combined via low-energy processing. However, CZTS-based solar cells still suffer from noncompetitive efficiencies (<13%).⁴⁹ Photoluminescence experiments measured poor minority carrier lifetimes,¹¹¹ which are often limited by the nonradiative Shockley–Reed–Hall (SRH) recombination process. Deep, midgap levels typically associated with defects and impurities¹¹² are typical culprits in SRH recombination. Thus, to improve the efficiency of CZTS-based cells, it is important to first understand the

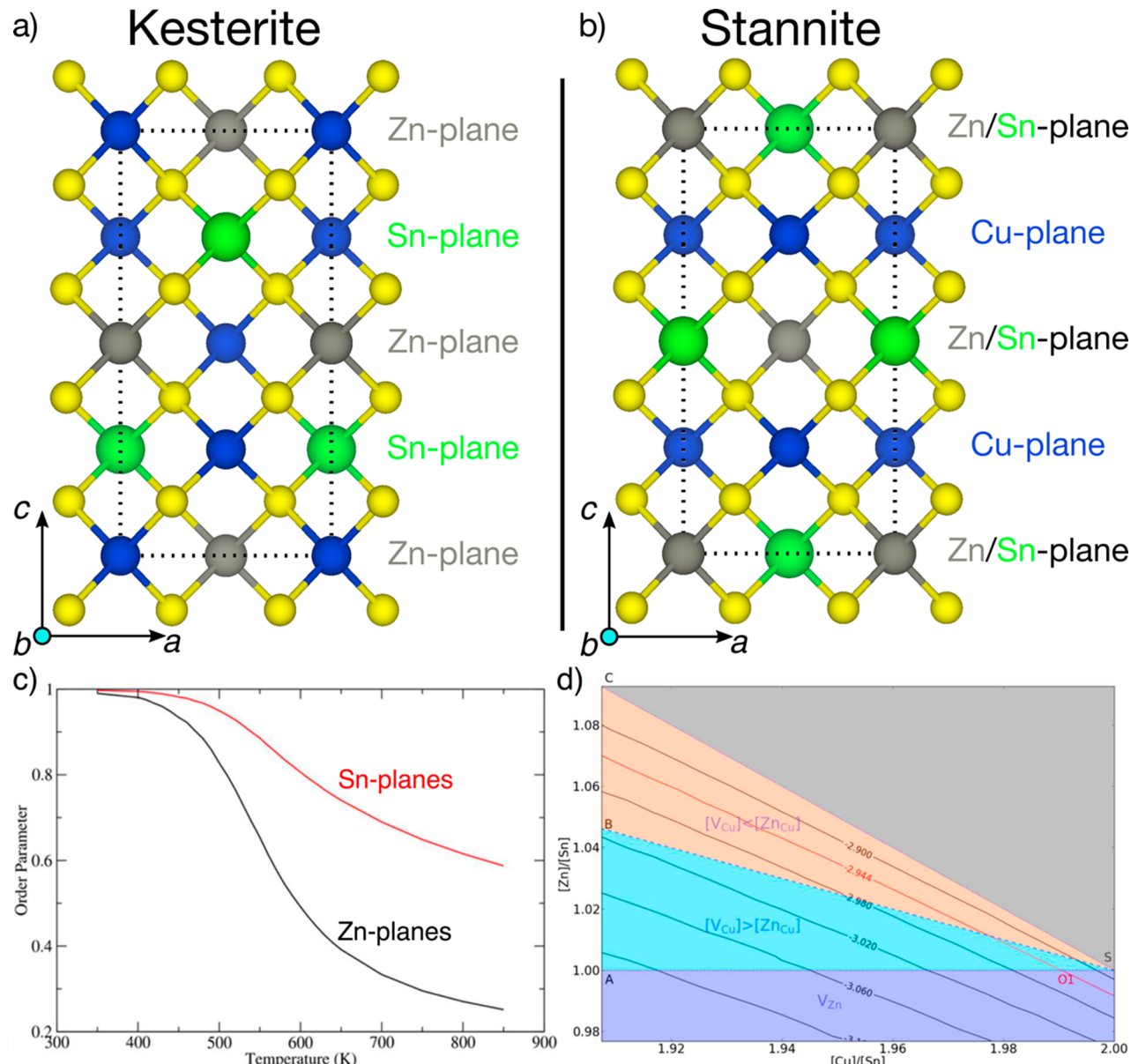


Figure 10. Structure of (a) kesterite and (b) stannite polymorphs of CZTS. Blue, green, gray, and yellow circles indicate Cu, Sn, Zn, and S atoms, respectively (reproduced from ref 53; copyright 2018 American Chemical Society). (c) Evolution of an order parameter along the Sn planes (red curve) and Zn planes (black curve) with temperature, obtained via Monte Carlo simulations (adapted from ref 52; copyright 2016 American Chemical Society). (d) Evolution of the Zn chemical potential in disordered CZTS at 750 K and 1 bar of S_8 , represented on a $[\text{Zn}]/[\text{Sn}]$ versus $[\text{Cu}]/[\text{Sn}]$ compositional space. See text for explanation of the various labeled points in panel d. Reproduced from ref 51. Copyright 2018 American Chemical Society.

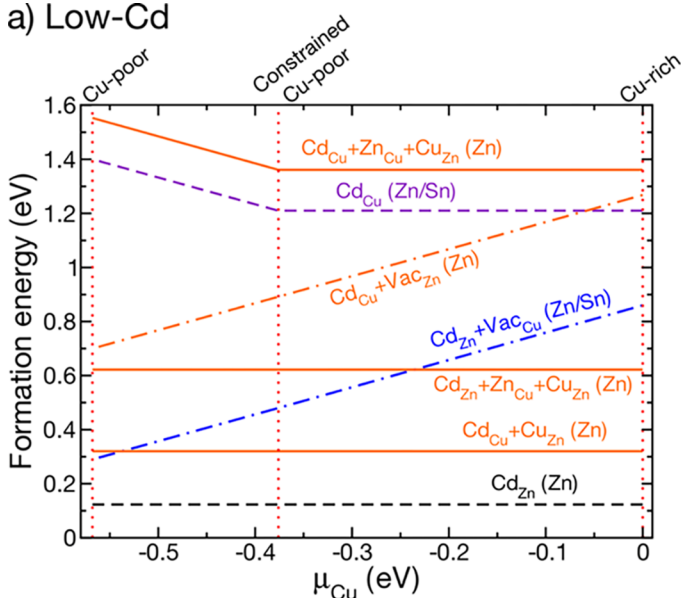
fundamental origins of defects within the CZTS structure and then develop strategies to mitigate them.

Figure 10a displays the most stable polymorph of CZTS, kesterite, while Figure 10b shows the stannite polymorph of CZTS, with blue, green, gray, and yellow circles signifying Cu, Sn, Zn, and S atoms, respectively. The primary difference between the two polymorphs is the stacking of the cations along the [001] direction (i.e., the *c*-direction in Figure 10a,b), with the kesterite exhibiting distinct Zn (+Cu) and Sn (+Cu) planes in contrast to Cu-only and Zn+Sn planes in stannite. Both PBE+*U*⁵⁰ and the strongly constrained appropriately normed (SCAN)⁵³ XC functionals predict a fairly small energy difference (~ 30 meV/fu) between the two polymorphs, highlighting their near-degeneracy. On the basis of cleavage

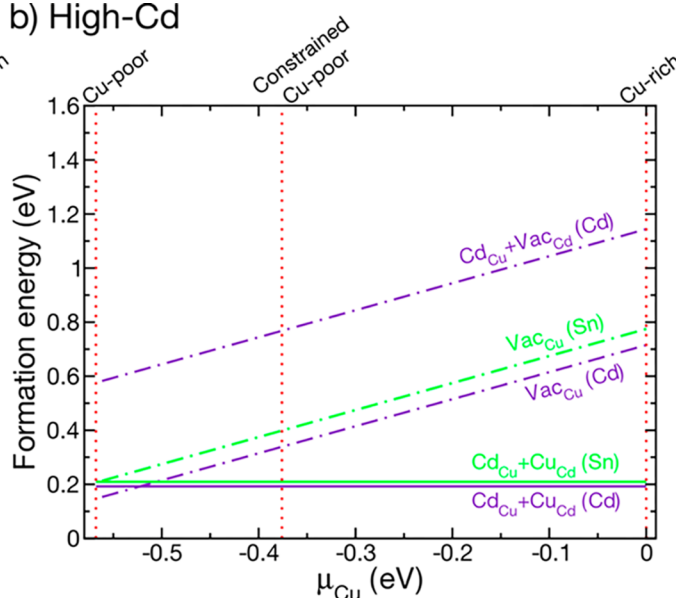
and interfacial energy calculations of the low-index surfaces of kesterite and stannite (using PBE+U+D2, where D2 corresponds to dispersion corrections¹¹³), Yu and Carter⁵⁰ suggested a possible means to stabilize the kesterite structure and allow for synthesis of nanoscale frameworks: use a Zn-terminated ZnS (001) surface as a template to grow CZTS crystals. Nevertheless, such small energy differences between the two polymorphs, coupled with the high-temperature annealing process used to introduce Se into the lattice¹¹⁴ during cell fabrication, often results in difficulties in synthesizing pure and ordered kesterite, frequently producing antisite and other defects.

To further understand the origin and extent of element disorder within the kesterite structure, Yu and Carter^{51,52}

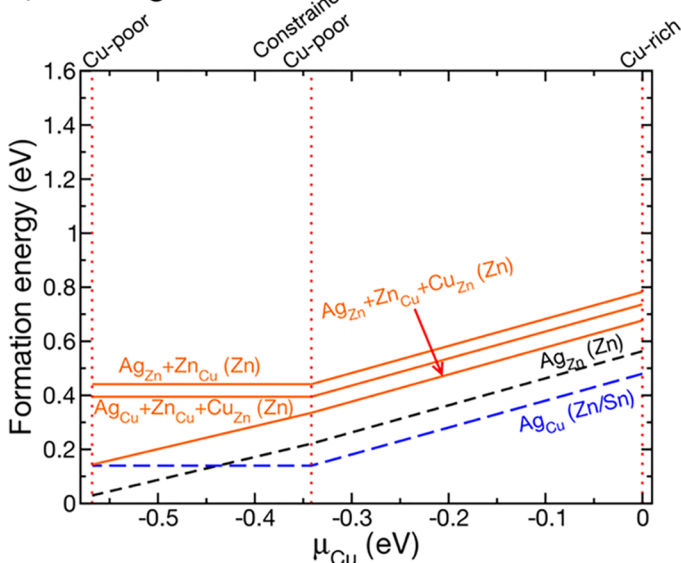
a) Low-Cd



b) High-Cd



c) Low-Ag



d) High-Ag

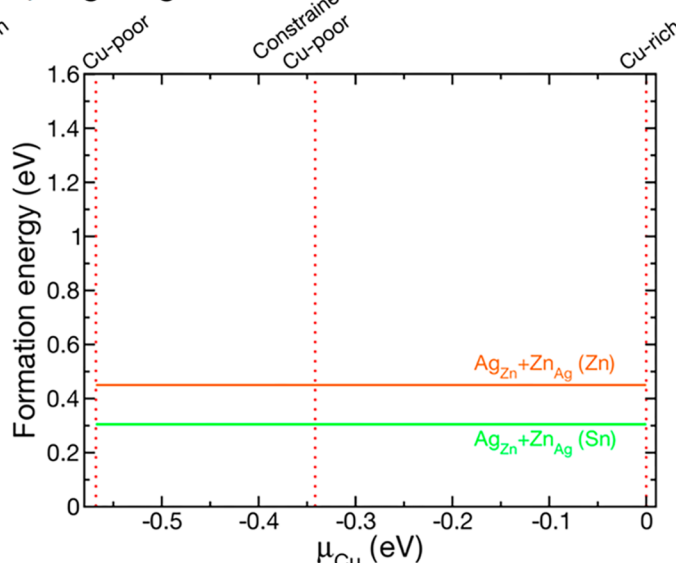


Figure 11. Formation energies of various point defects in kesterite CZTS are plotted against the Cu chemical potential (μ_{Cu}) under (a) low Cd, (b) high Cd, (c) low Ag, and (d) high Ag doping conditions. Solid lines refer to defects that represent disorder within the kesterite. Dashed lines represent the energy required to dope Cd or Ag within CZTS, while dash-dot lines correspond to the formation energies of Cu vacancies (Vac_{Cu}). See text for explanation of the text legends within each panel and the various μ_{Cu} considered. Adapted from ref 53. Copyright 2018 American Chemical Society.

constructed a cluster expansion (CE; see the Supporting Information)¹¹⁵ model based on PBE+*U* calculations and subsequently performed Monte Carlo (MC) simulations to observe the temperature dependence of order (Figure 10c) within the kesterite lattice. Figure 10c plots a global order parameter (*O*) across Zn planes (black curve) and Sn planes (red curve) within the kesterite structure, as a function of temperature. Note that a perfectly ordered kesterite has *O* = 1.0 for both the Zn and Sn planes. In the case of disorder in the Zn planes only, *O* ~ 0.0 (1.0) for the Zn (Sn) planes, while a completely random kesterite (i.e., disorder in both the Zn and Sn planes) formally exhibits *O* ~ 0.0 and 0.11 for the Zn and Sn planes, respectively. Across typical annealing temperatures (500–800 K^{114,116}), the order parameter is quite different from both the perfectly ordered (*O* = 1.0) and the completely

random ($O_{\text{Zn}} = 0.0$, $O_{\text{Sn}} = 0.11$) kesterite, suggesting a significant amount of short-range disorder on both the Zn and Sn planes. Furthermore, PBE+*U* band gap estimates indicate that the band gap in disordered structures (at 750 K) could drop deleteriously by about ~0.3 eV compared to that of the ordered structure (at 0 K).⁵²

Given the thermodynamic origins of disorder within the kesterite structure, the synthesis and fabrication of CZTS must be controlled precisely to enhance efficiencies. The highest efficiencies are found when CZTS is synthesized under Cu-poor and Zn-rich conditions ($[\text{Cu}]/[\text{Sn}] \sim 1.98$ and $[\text{Zn}]/[\text{Sn}] \sim 1.2$,^{117,118} where [X] refers to the concentration of X within the kesterite). To explore the extent to which Cu-poor and Zn-rich conditions can be enforced during CZTS synthesis, Yu and Carter⁵¹ generated chemical potential

maps across the $[Zn]/[Sn]$ versus $[Cu]/[Sn]$ compositional space. The authors⁵¹ extended their CE model and developed a test particle deletion (TPD)¹¹⁹-based umbrella sampling scheme to estimate chemical potentials in disordered supercells during MC simulations.

Figure 10d plots the evolution of the Zn chemical potential (μ_{Zn}) across various $[Zn]/[Sn]$ and $[Cu]/[Sn]$ ratios relevant to CZTS at 750 K and using S_8 at 1 bar as the reference for the chemical potential of S (μ_S). The label S in **Figure 10d**, corresponding to $[Cu]/[Sn] = 2$ and $[Zn]/[Sn] = 1$, marks stoichiometric CZTS. The gray region above the dotted “C–S” line indicates compositions of excess Cu + Zn, rather than stoichiometric CZTS, and are not relevant for chemical potential estimations. The purple region below the dotted “A–S” line corresponds to a Zn-poor stoichiometry with Zn vacancies (V_{Zn}), while the orange (ΔCBS) and blue (ΔABS) regions are dominated respectively by “excess-Zn_{Cu}” antisites and Cu vacancies (V_{Cu}). Note that excess-Zn_{Cu} is the net $[Zn_{Cu}] - [Cu_{Zn}]$ antisite content and directly reflects the free electron ($[e^-]$) concentration. The “B–S” line, indicating $[V_{Cu}] - \text{excess-Zn}_{Cu} = 0$, therefore signifies no free carriers (i.e., $[h^+] \equiv [e^-]$) in the dark, with the blue (orange) region reflecting excess holes (electrons) and a p(n)-type behavior. In addition to experiments reporting the highest efficiencies under Cu-poor and Zn-rich conditions, prior work by Yu and Carter⁵² also indicated that V_{Cu} can enhance the efficiencies of CZTS by introducing delocalized holes and mitigating local band gap fluctuations within kesterite, while V_{Zn} is known to act as hole traps.¹²⁰ CZTS synthesis therefore must be optimized such that $[h^+]$ is maximized, which is equivalent to maximizing $[V_{Cu}] - \text{excess-Zn}_{Cu}$. Since $[h^+]$ increases with decreasing y -intercept in **Figure 10d**, maximizing $[h^+]$ is equivalent to finding an experimentally accessible line parallel to “B–S” with the lowest $[Zn]/[Sn]$. Lines parallel to “B–S” have constant hole concentration, so for a given hole concentration, we can identify the limiting $[Cu]/[Sn]$ and $[Zn]/[Sn]$ ratios. Finally, the red isoline in **Figure 10d** indicates that $\mu_{Zn} = \mu_{Zn}^{ZnS}$, which corresponds to Zn-rich conditions during synthesis. Consequently, “O1” in **Figure 10d** indicates the highest $[h^+]$ that can be achieved under Zn-rich conditions during synthesis and is equivalent to $[Zn]/[Sn] \sim 1$ and $[Cu]/[Sn] \sim 1.995$, in qualitative agreement with experimental observations.¹¹⁸

Stoichiometry constraints due to secondary Sn phases impose a lower bound for $[Cu]/[Sn]$ of ~ 1.985 at $[Zn]/[Sn] \sim 1$ (i.e., Zn-rich conditions),⁵¹ resulting in a variation between 0.005 and 0.015 in $[V_{Cu}]$. The extent of variation in $[V_{Cu}]$ decreases with decreasing temperature,⁵¹ indicating that higher-temperature annealing conditions favor $[V_{Cu}]$ formation, albeit with increasing disorder. Also, $[V_{Cu}]$ increases with increasing μ_S ,⁵¹ suggesting that more reactive sulfurization conditions might improve CZTS performance. Thus, Yu and Carter⁵¹ identified the optimal synthesis conditions for CZTS, namely, Zn-rich and Sn-rich conditions, to maximize $[h^+]$ and efficiencies, and also quantified the possible variations in $[V_{Cu}]$ within kesterite.

Aside from calibrating the synthesis conditions, another strategy to mitigate lattice disorder is to employ isovalent dopants that penalize formation of disorder-inducing antisites, such as Cu_{Zn} and Zn_{Cu}. Since Cu⁺ and Zn²⁺ have similar ionic radii ($\sim 0.6 \text{ \AA}$)⁸⁸ that facilitate formation of Cu_{Zn} and Zn_{Cu}, doping isovalent ions that are significantly different in size, such as Cd²⁺ ($\sim 0.78 \text{ \AA}$) on Zn²⁺ sites and Ag⁺ ($\sim 1 \text{ \AA}$) on Cu⁺

sites, might suppress antisite formation. Although improved open circuit voltage (V_{oc}) and efficiencies have been observed with both Cd and Ag doping^{121–123} of CZTS, Cd and Ag doping achieve rather low peak efficiencies ($\sim 11\%$ efficiency at 40% Cd and $\sim 9.8\%$ efficiency at 3–5% Ag). To gain greater understanding of the effect of these dopants, Gautam et al.⁵³ evaluated bulk and defect energetics (using DFT-SCAN) and electronic structures (using PBE+U+D2) of Cd- and Ag-doped kesterite at low and high levels of doping, building upon previous theoretical studies.^{30,120,124}

Figure 11 plots the formation energies of various defects within the kesterite structure against Cu chemical potential (μ_{Cu}) at low and high Cd doping (panels a and b) and low and high Ag-doping (c and d), respectively. The low doping of Cd and Ag here corresponds to a concentration, $x_{Cd} = x_{Ag} \sim 0.015$ per S, while the high doping here signifies $x_{Cd} \sim 0.125$ and $x_{Ag} \sim 0.25$ per S, respectively. Three distinct chemical scenarios emerge as μ_{Cu} varies (dotted red-lines in **Figure 11**), namely, (i) Cu-rich (CZTS in equilibrium with bulk Cu, ZnS (Zn-rich phase), and SnS (Sn-rich)); (ii) constrained Cu-poor (ZnS and SnS in equilibrium with CZTS alongside Cu-deficient phases); and (iii) Cu-poor (the lowest μ_{Cu} at which CZTS can be stable without any additional constraints). The solid, dashed, and dash-dot lines in **Figure 11** represent the disorder-inducing defects, the ease of doping either Cd or Ag, and the ease of formation of Cu vacancies (Vac_{Cu}), respectively. Legends (Sn), (Zn), and (Zn/Sn) represent the formation of the corresponding defect on the Sn, Zn, and either Zn or Sn planes of kesterite, respectively. The authors⁵³ reported that the disorder-inducing defects in the pure kesterite had a formation energy of $\sim 0.22\text{--}0.25 \text{ eV}$ (in agreement with previous studies¹²⁰), which is a useful benchmark to compare with the effectiveness of Cd and Ag doping.

Interestingly, Cd and Ag display contrasting behaviors as dopants within CZTS. For example, Cd clearly prefers Zn sites upon doping (formation energy of Cd_{Zn} $\sim 0.12 \text{ eV}$ versus Cd_{Cu} $\sim 1.21\text{--}1.4 \text{ eV}$, **Figure 11a**), while Ag prefers to occupy Zn sites over Cu at Cu-poor conditions (Ag_{Zn} $\sim 0.03 \text{ eV}$ versus Ag_{Cu} $\sim 0.14 \text{ eV}$, **Figure 11c**). Similarly, Cd and Ag suppress disorder-inducing defects under different doping conditions. For example, the disorder-inducing antisites (solid orange lines in **Figure 11a**) at low Cd doping exhibit higher formation energies ($\sim 0.32\text{--}1.55 \text{ eV}$) than that of pure kesterite ($\sim 0.22\text{--}0.25 \text{ eV}$), while high Cd doping does not actively suppress detrimental antisites ($\sim 0.19\text{--}0.21 \text{ eV}$, solid lines in **Figure 11b**). In the case of Ag, higher Ag content suppresses disorder ($\sim 0.30\text{--}0.45 \text{ eV}$, solid lines in **Figure 11d**) across μ_{Cu} while low Ag doping penalizes disorder under constrained Cu-poor to Cu-rich conditions only ($\sim 0.34\text{--}0.78 \text{ eV}$, solid orange lines in **Figure 11c**). Additionally, Gautam et al. reported that increasing the Cd (Ag) concentration within CZTS stabilizes the stannite (kesterite) polymorph,⁵³ consequently decreasing (increasing) the band gap of CZTS. Cd and Ag therefore improve the V_{oc} and efficiency of CZTS solar cells via different mechanisms. The contrasting influences on the defect and bulk properties by the dopants are likely to be responsible for the observation of a peak efficiency in the doped cells.

In summary, lattice disorder within kesterite due to the near-degeneracy of the kesterite and stannite polymorphs is the primary cause of low efficiencies observed in CZTS-based solar cells. Indeed, CE-MC simulations confirm that significant disorder can exist within kesterite at typical annealing temperatures (500–800 K). Furthermore, usage of Zn- and

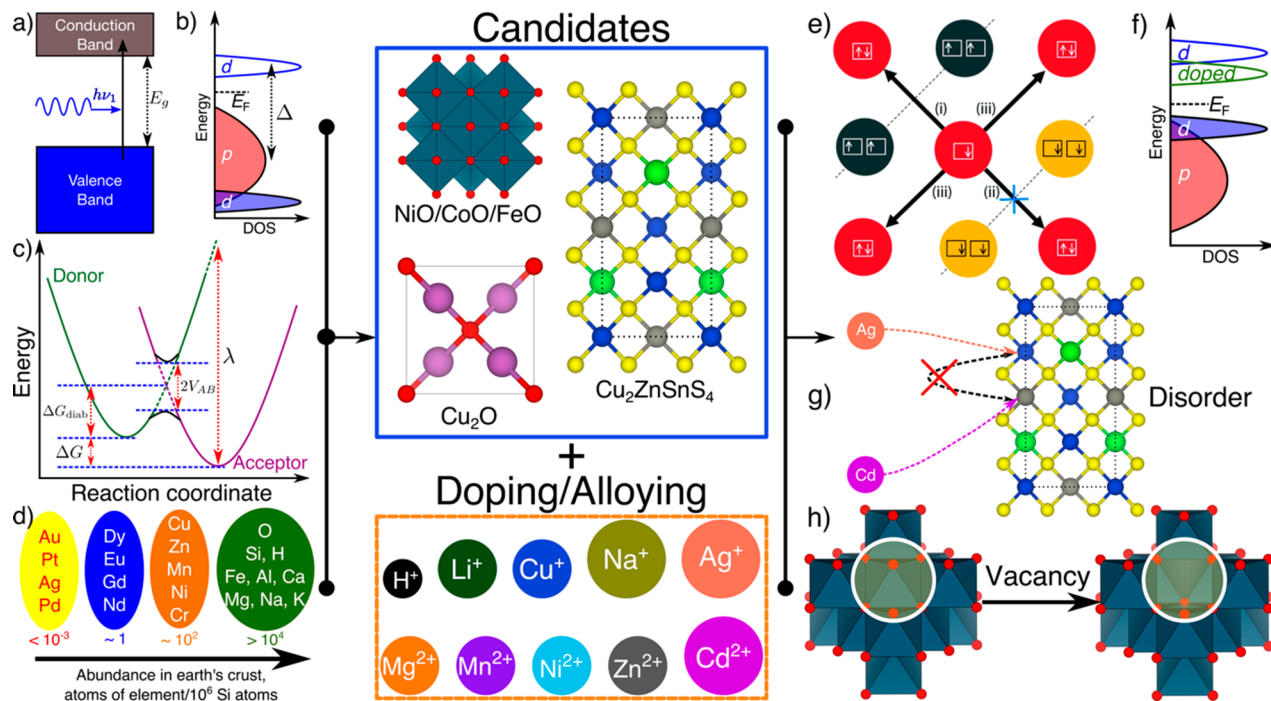


Figure 12. Schematic of the various requirements for materials to be used in solar applications (panels a–d), the candidates discussed in this work, and the impact of doping and/or alloying on the improved charge transport (panel e), electronic properties (f), and bulk stability (g, h) of the materials considered. Data for panel d taken from ref 125 Panels a, e, and g adapted from ref 5 (Copyright 2016 American Institute of Physics), ref 42 (Copyright 2015 Royal Society of Chemistry), and ref 53 (Copyright 2018 American Chemical Society), respectively.

Sn-rich conditions during CZTS synthesis is crucial for reducing both the intrinsic disorder and facilitating formation of beneficial Cu vacancies. Finally, isovalent dopants, e.g., Cd²⁺ and Ag⁺, can improve efficiencies of CZTS-based cells under different doping and chemical conditions, but neither dopant produces improvements at the level desired, indicating the need to find more effective dopants.

5. DISCUSSION

The development of novel, beyond-Si PV materials, which has been the focus of this review, requires simultaneously satisfying several constraints as schematically described in panels a–d of Figure 12. Specifically, the PV should exhibit (i) an ideal band gap (~1.5 eV, Figure 12a, section 2) in the light-absorbing semiconductor; (ii) low carrier-recombination rates, such as in a CT insulator (relevant for TCOs and the light-absorbing semiconductor, Figure 12b, section 2); (iii) rapid transport of photogenerated carriers (e.g., Figure 12c typical of small polaron hopping in TMOs, section 3); (iv) stability (section 4); and (v) environmentally friendly constituents (Figure 12d). Notably, all of the materials reviewed here, including NiO, CoO, FeO, Cu₂O, and CZTS (blue rectangle in Figure 12), are made of abundant, environmentally friendly elements; the semiconductors themselves are fairly inexpensive to process, thus satisfying one of the aforementioned requirements (Figure 12d).

However, all of the candidate materials suffer from major drawbacks that cause severe limitations in their corresponding performance and therefore a lack of successful commercialization thus far. For example, the intermediate band gap of CoO is too narrow for high-efficiency IBPVs. NiO and FeO exhibit low intrinsic hole mobility, while Cu₂O-based PV devices are detrimentally affected by hole traps. In the case of CZTS, the antisite-induced lattice disorder introduces deep, midgap

states, resulting in a performance reduction in solar cells. The use of computational tools is particularly important in understanding the fundamental origins of such performance-limiting factors and in discovering potential improvement strategies.

In terms of theoretical methods for evaluating material properties (described in detail in the Supporting Information), we find DFT-based calculations generally to be sufficient in describing ground-state energetics for pure and doped transition-metal oxides^{47,81} and CZTS.^{50,53} Specifically, either the GGA or the SCAN XC functional, with an appropriately determined Hubbard $U^{93,126}$ added on transition-metal centers, describes the XC interactions fairly well and provides excellent agreement with experimental thermodynamic quantities. As a recently developed functional, the accuracy of SCAN for predicting bulk and defect energetics is still an active area of research.¹²⁶ However, we suggest the use of excited-state methods, including non-self-consistent G_0W_0 , for band gap predictions that are directly comparable to PES/IPES measurements,^{5,39} unless there is strong evidence of either DFT(+U) or hybrid functionals yielding reliable qualitative trends.⁴¹ For modeling charge transport, a simple ground-state theory, such as UHF calculations (on electrostatically embedded clusters; see the Supporting Information) can yield reasonable diabatic barriers,^{40,42,43} while correlated-wavefunction methods, e.g., CASSCF, will be required to precisely estimate adiabatic barriers.^{40,42} Thus, the reader should be aware that different theoretical frameworks are required to obtain accurate predictions for specific properties of specific materials classes, as summarized also in other reviews,^{21,127–129} and careful benchmarking of the selected theoretical approach against available experimental data must be done to validate a given choice of theory for a given property or material class.

Theoretical predictions indicate that doping and/or alloying with an *optimal* element (orange box in Figure 12) is a viable strategy for significantly improving the properties of all materials considered in this work (panels e–g in Figure 12). With respect to band structure engineering, Li-alloyed NiO exhibits a band gap in the visible range of the solar spectrum (Figure 2), potentially expanding the versatility of NiO for use as a light absorber. However, alloying CoO with NiO preserves the double-gap electronic structure besides improving the width of the intermediate band (by ~0.7 eV, Figure 3), which could be useful for IBPVs or multispectral LEDs. Additionally, alloying FeO with ZnO reduces the band gap to optimal values for PV light absorption (~1.5 eV at $\text{Fe}_{0.5}\text{Zn}_{0.5}\text{O}$) and introduces a CT character to the band edges, potentially reducing carrier-recombination rates (schematic in Figure 12f).

With respect to charge transport tailoring, homogeneous alloying of NiO with MgO or ZnO can reduce the barrier and anisotropy to enable 3-D hole conductivity in NiO (Table 1, Figure 12e), while both p- (Li^+ , Na^+) and n-doping (H^+ interstitials) in FeO can enhance hole transport (Table 2). With respect to intrinsic defects and bulk stability of candidate materials, theory predicts that alloying FeO with isovalent metal oxides (ZnO and NiO) can improve the bulk stability of FeO, suppressing cation vacancy formation (Figure 4 and Figure 12h). However, the concentration of the intrinsic hole trap in Cu_2O , $V_{\text{Cu}}^{\text{split}}$ (Figure 9d), can be substantially reduced via both the isovalent (Li^+) and n-doping (MgO, MnO, ZnO) of Cu_2O (Table 3). Isovalent doping is preferable, as n-doping will reduce the number of charge carriers and hence the overall conductivity. The high degree of performance-reducing lattice disorder in CZTS (Figure 12g), caused by $\text{Cu}_{\text{Zn}}+\text{Zn}_{\text{Cu}}$ antisites (Figure 10c), can be mitigated via isovalent doping of Ag^+ (on Cu^+) or Cd^{2+} (on Zn^{2+} , Figure 11).

Additionally, chemical conditions during either synthesis or operation can have a substantial impact on the performance of the material in a solar application. For example, Cu-poor conditions during synthesis of Cu_2O may increase the concentration of $V_{\text{Cu}}^{\text{split}}$ trap sites, as indicated by a decrease in the formation energy of the analogous V_{Cu} (Table 3). Similarly, Zn-rich and Sn-rich conditions may stabilize the kesterite structure of CZTS (Figure 10d), while Cu-rich conditions are needed to make low Ag doping effective (Figure 11c). Also, Fe-poor conditions during the synthesis of FeO naturally can increase the concentration of V_{Fe} , potentially increasing the intrinsic hole concentration.⁹⁰ Thus, a combination of employing appropriate synthesis conditions and meticulous doping may lead to the successful deployment of TMOs and kesterite sulfides in commercial solar applications.

6. CONCLUSIONS

We reviewed theoretical work on two classes of materials, namely, TMOs (NiO, CoO, Cu_2O , and FeO) and kesterite sulfides (CZTS), which are promising candidates for novel solar applications. Carter and co-workers used a wide range of QM-based methods to understand the electronic properties, charge transport, and bulk and defect energetics in candidate materials, proposing strategies for improvement. Specifically, doping and/or alloying was shown to improve (i) electronic properties in NiO, CoO, and FeO; (ii) hole transport in NiO and FeO; (iii) bulk stability of FeO; and (iv) suppression of performance-limiting defects in Cu_2O and CZTS. Given the need for improving the energy efficiency and cost of PV technologies to ensure a sustainable fossil-free future, we hope

that this review may act as a guide to both theorists and experimentalists in the search for and improvement of new materials for solar energy applications.

■ ASSOCIATED CONTENT

■ Supporting Information

The Supporting Information is available free of charge on the ACS Publications website at DOI: 10.1021/acs.jpcc.8b08185.

Overview of the various theoretical methods used for calculating the different material properties that are described in this work (PDF)

■ AUTHOR INFORMATION

Corresponding Author

*E.A. Carter. E-mail: eac@princeton.edu.

ORCID

Gopalakrishnan Sai Gautam: 0000-0002-1303-0976

Thomas P. Senftle: 0000-0002-5889-5009

Emily A. Carter: 0000-0001-7330-7554

Present Addresses

[†]Department of Chemical and Biomolecular Engineering, Rice University, Houston, TX 77005.

[‡]Rigetti Computing, 2919 7th Street, Berkeley, CA 94710.

Notes

The authors declare no competing financial interest.

Biographies

Gopalakrishnan Sai Gautam has been a Postdoctoral Research Associate in Mechanical and Aerospace Engineering at Princeton University since July 2017 in the group of Dean Emily A. Carter. He completed his Ph.D. in Materials Science and Engineering at Massachusetts Institute of Technology during the summer of 2017 working on electrode materials for multivalent batteries. Currently, he focuses on using computational tools to optimize and design novel materials for photovoltaic and solar thermochemical applications.

Thomas P. Senftle is an Assistant Professor in Chemical and Biomolecular Engineering at Rice University since 2017. He earned his Ph.D. in Chemical Engineering at The Pennsylvania State University in 2015 working on metal-oxide catalysts for hydrocarbon activation. He completed postdoctoral research at Princeton University in Dean Emily A. Carter's group working on the computational design of functionalized semiconductors for photoelectrochemical applications. His current research focuses on the development and application of computational modeling tools for assessing complex, multicomponent interfaces between semiconductor surfaces and electrolyte solutions.

Nima Alidoust is a Product Manager at Rigetti Computing, a full-stack quantum computing start-up in Berkeley, California. He received his Ph.D. in Electrical Engineering from Princeton under the supervision of Dean Emily A. Carter. His Ph.D. work primarily focused on application of electronic structure theory in discovering and optimizing novel materials for solar energy conversion. After completing his Ph.D., he joined McKinsey & Co's Northeastern Office, where he worked with semiconductor, renewable energy, and advanced electronic clients on strategy and innovation. He is currently part of the Ecosystem Development and Product teams at Rigetti Computing, leading Rigetti's strategic partnerships.

Emily A. Carter is the Dean of the School of Engineering and Applied Science, Gerhard R. Andlinger Professor in Energy and the Environment, and Professor of Mechanical and Aerospace Engineering and Computational Mathematics at Princeton

University. Her research focuses on developing and applying accurate, efficient quantum mechanics methods that enable the discovery and design of materials for sustainable energy. From 2010 to 2016, she was the Founding Director of Princeton's Andlinger Center for Energy and the Environment. She has been a member of the Princeton faculty since 2004; before that, she spent 16 years on the faculty at UCLA. She is a member of the National Academy of Sciences, the American Academy of Arts and Sciences, and the National Academy of Engineering, among other honors.

ACKNOWLEDGMENTS

E.A.C. thanks the U.S. Department of Energy, Office of Science, Basic Energy Sciences under Award No. DE-SC0002120 for funding this project. The authors thank Ms. Nari L. Baughman for a careful reading of the manuscript.

REFERENCES

- (1) NREL. Research cell efficiency records chart <https://www.nrel.gov/pv/assets/images/efficiency-chart.png> (accessed Jul 15, 2018).
- (2) Green, M. A.; Emery, K.; Hishikawa, Y.; Warta, W.; Dunlop, E. D. Solar Cell Efficiency Tables (Version 45). *Prog. Photovoltaics* **2015**, *23*, 1–9.
- (3) Branker, K.; Pathak, M. J. M.; Pearce, J. M. A Review of Solar Photovoltaic Levelized Cost of Electricity. *Renewable Sustainable Energy Rev.* **2011**, *15*, 4470–4482.
- (4) Shockley, W.; Queisser, H. J. Detailed Balance Limit of Efficiency of P-n Junction Solar Cells. *J. Appl. Phys.* **1961**, *32*, 510–519.
- (5) Alidoust, N.; Lessio, M.; Carter, E. A. Cobalt (II) Oxide and Nickel (II) Oxide Alloys as Potential Intermediate-Band Semiconductors: A Theoretical Study. *J. Appl. Phys.* **2016**, *119*, 025102.
- (6) Miller, O. D.; Yablonovitch, E.; Kurtz, S. R. Strong Internal and External Luminescence as Solar Cells Approach the Shockley–Queisser Limit. *IEEE J. Photovoltaics* **2012**, *2*, 303–311.
- (7) Gloeckler, M.; Sankin, I.; Zhao, Z. CdTe Solar Cells at the Threshold to 20% Efficiency. *IEEE J. Photovoltaics* **2013**, *3*, 1389–1393.
- (8) Jackson, P.; Hariskos, D.; Wuerz, R.; Kiowski, O.; Bauer, A.; Friedlmeier, T. M.; Powalla, M. Properties of Cu(In,Ga)Se₂ Solar Cells with New Record Efficiencies up to 21.7%. *Phys. Status Solidi RRL* **2015**, *9*, 28–31.
- (9) Yang, W. S.; Noh, J. H.; Jeon, N. J.; Kim, Y. C.; Ryu, S.; Seo, J.; Seok, S. I. High-Performance Photovoltaic Perovskite Layers Fabricated through Intramolecular Exchange. *Science* **2015**, *348*, 1234–1237.
- (10) Pascual, J.; Delgado, J. L.; Tena-Zaera, R. Physicochemical Phenomena and Application in Solar Cells of Perovskite:Fullerene Films. *J. Phys. Chem. Lett.* **2018**, *9*, 2893–2902.
- (11) Marinova, N.; Valero, S.; Delgado, J. L. Organic and Perovskite Solar Cells: Working Principles, Materials and Interfaces. *J. Colloid Interface Sci.* **2017**, *488*, 373–389.
- (12) Yamaguchi, M. III–V Compound Multi-Junction Solar Cells. *Sol. Energy Mater. Sol. Cells* **2003**, *75*, 261–269.
- (13) Luque, A.; Martí, A. Increasing the Efficiency of Ideal Solar Cells by Photon Induced Transitions at Intermediate Levels. *Phys. Rev. Lett.* **1997**, *78*, 5014–5017.
- (14) Thompson, A. G.; Woolley, J. C. Energy-Gap Variation In Mixed III–V Alloys. *Can. J. Phys.* **1967**, *45*, 255–261.
- (15) Dimroth, F.; Kurtz, S. High-Efficiency Multijunction Solar Cells. *MRS Bull.* **2007**, *32*, 230–235.
- (16) Grätzel, M. Dye-Sensitized Solar Cells. *J. Photochem. Photobiol., C* **2003**, *4*, 145–153.
- (17) Irwin, M. D.; Buchholz, D. B.; Hains, A. W.; Chang, R. P. H.; Marks, T. J. P-Type Semiconducting Nickel Oxide as an Efficiency-Enhancing Anode Interfacial Layer in Polymer Bulk-Heterojunction Solar Cells. *Proc. Natl. Acad. Sci. U. S. A.* **2008**, *105*, 2783–2787.
- (18) Bush, K. A.; Bailie, C. D.; Chen, Y.; Bowring, A. R.; Wang, W.; Ma, W.; Leijtens, T.; Moghadam, F.; McGehee, M. D. Thermal and Environmental Stability of Semi-Transparent Perovskite Solar Cells for Tandems Enabled by a Solution-Processed Nanoparticle Buffer Layer and Sputtered ITO Electrode. *Adv. Mater.* **2016**, *28*, 3937–3943.
- (19) Fortunato, E.; Ginley, D.; Hosono, H.; Paine, D. C. Transparent Conducting Oxides for Photovoltaics. *MRS Bull.* **2007**, *32*, 242–247.
- (20) Minami, T. Present Status of Transparent Conducting Oxide Thin-Film Development for Indium-Tin-Oxide (ITO) Substitutes. *Thin Solid Films* **2008**, *516*, 5822–5828.
- (21) Carter, E. A. Challenges in Modeling Materials Properties Without Experimental Input. *Science* **2008**, *321*, 800–803.
- (22) Lejaeghere, K.; Bihlmayer, G.; Bjorkman, T.; Blaha, P.; Blugel, S.; Blum, V.; Caliste, D.; Castelli, I. E.; Clark, S. J.; Dal Corso, A.; et al. Reproducibility in Density Functional Theory Calculations of Solids. *Science* **2016**, *351*, 6280.
- (23) Canepa, P.; Sai Gautam, G.; Hannah, D. C.; Malik, R.; Liu, M.; Gallagher, K. G.; Persson, K. A.; Ceder, G. Odyssey of Multivalent Cathode Materials: Open Questions and Future Challenges. *Chem. Rev.* **2017**, *117*, 4287–4341.
- (24) Liao, P.; Carter, E. A. New Concepts and Modeling Strategies to Design and Evaluate Photo-Electro-Catalysts Based on Transition Metal Oxides. *Chem. Soc. Rev.* **2013**, *42*, 2401–2422.
- (25) Nørskov, J. K.; Bligaard, T.; Rossmeisl, J.; Christensen, C. H. Towards the Computational Design of Solid Catalysts. *Nat. Chem.* **2009**, *1*, 37–46.
- (26) Urban, A.; Seo, D.-H.; Ceder, G. Computational Understanding of Li-Ion Batteries. *npj Comput. Mater.* **2016**, *2*, 16002.
- (27) Dieterich, J. M.; Carter, E. A. Opinion: Quantum Solutions for a Sustainable Energy Future. *Nat. Rev. Chem.* **2017**, *1*, 0032.
- (28) Yang, J.; Sudik, A.; Wolverton, C.; Siegel, D. J. High Capacity Hydrogen Storage Materials: Attributes for Automotive Applications and Techniques for Materials Discovery. *Chem. Soc. Rev.* **2010**, *39*, 656–675.
- (29) van Santen, R. A.; Neurock, M. *Molecular Heterogeneous Catalysis*; Wiley-VCH Verlag GmbH & Co. KGaA: Weinheim, Germany, 2006.
- (30) Walsh, A.; Chen, S.; Wei, S.-H.; Gong, X.-G. Kesterite Thin-Film Solar Cells: Advances in Materials Modelling of Cu₂ZnSnS₄. *Adv. Energy Mater.* **2012**, *2*, 400–409.
- (31) Hohenberg, P.; Kohn, W. Inhomogeneous Electron Gas. *Phys. Rev.* **1964**, *136*, B864–B871.
- (32) Kohn, W.; Sham, L. J. Self-Consistent Equations Including Exchange and Correlation Effects. *Phys. Rev.* **1965**, *140*, A1133–A1138.
- (33) Hybertsen, M. S.; Louie, S. G. First-Principles Theory of Quasiparticles: Calculation of Band Gaps in Semiconductors and Insulators. *Phys. Rev. Lett.* **1985**, *55*, 1418–1421.
- (34) Li, X.-Z.; Gómez-Abal, R.; Jiang, H.; Ambrosch-Draxl, C.; Scheffler, M. Impact of Widely Used Approximations to the G₀W₀ Method: An All-Electron Perspective. *New J. Phys.* **2012**, *14*, 023006.
- (35) Amos, T.; Snyder, L. C. Unrestricted Hartree–Fock Calculations. I. An Improved Method of Computing Spin Properties. *J. Chem. Phys.* **1964**, *41*, 1773–1783.
- (36) Roos, B. O. The Complete Active Space SCF Method in a Fock-Matrix-Based Super-CI Formulation. *Int. J. Quantum Chem.* **1980**, *18*, 175–189.
- (37) Coker, E. N.; Rodriguez, M. A.; Ambrosini, A.; Miller, J. E.; Stechel, E. B. Using In-Situ Techniques to Probe High-Temperature Reactions: Thermochemical Cycles for the Production of Synthetic Fuels from CO₂ and Water. *Powder Diffr.* **2012**, *27*, 117–125.
- (38) Chavez-Galan, J.; Almanza, R. Solar Filters Based on Iron Oxides Used as Efficient Windows for Energy Savings. *Sol. Energy* **2007**, *81*, 13–19.
- (39) Alidoust, N.; Toroker, M. C.; Keith, J. A.; Carter, E. A. Significant Reduction in NiO Band Gap Upon Formation of

- $\text{Li}_x\text{Ni}_{1-x}\text{O}$ Alloys: Applications To Solar Energy Conversion. *ChemSusChem* **2014**, *7*, 195–201.
- (40) Alidoust, N.; Carter, E. A. Three-Dimensional Hole Transport in Nickel Oxide by Alloying with MgO or ZnO. *J. Appl. Phys.* **2015**, *118*, 185102.
- (41) Toroker, M. C.; Carter, E. A. Transition Metal Oxide Alloys as Potential Solar Energy Conversion Materials. *J. Mater. Chem. A* **2013**, *1*, 2474.
- (42) Alidoust, N.; Carter, E. A. First-Principles Assessment of Hole Transport in Pure and Li-Doped NiO. *Phys. Chem. Chem. Phys.* **2015**, *17*, 18098–18110.
- (43) Toroker, M. C.; Carter, E. A. Hole Transport in Non-stoichiometric and Doped Wüstite. *J. Phys. Chem. C* **2012**, *116*, 17403–17413.
- (44) Darken, L. S.; Gurry, R. W. The System Iron-Oxygen. I. The Wüstite Field and Related Equilibria. *J. Am. Chem. Soc.* **1945**, *67*, 1398–1412.
- (45) Toroker, M. C.; Carter, E. A. Strategies to Suppress Cation Vacancies in Metal Oxide Alloys: Consequences for Solar Energy Conversion. *J. Mater. Sci.* **2015**, *50*, 5715–5722.
- (46) Rai, B. P. Cu₂O Solar Cells: A Review. *Sol. Cells* **1988**, *25*, 265–272.
- (47) Isseroff, L. Y.; Carter, E. A. Electronic Structure of Pure and Doped Cuprous Oxide with Copper Vacancies: Suppression of Trap States. *Chem. Mater.* **2013**, *25*, 253–265.
- (48) Delbos, S. Kesterite Thin Films for Photovoltaics: A Review. *EPJ Photovoltaics* **2012**, *3*, 35004.
- (49) Wang, W.; Winkler, M. T.; Gunawan, O.; Gokmen, T.; Todorov, T. K.; Zhu, Y.; Mitzi, D. B. Device Characteristics of CZTSSe Thin-Film Solar Cells with 12.6% Efficiency. *Adv. Energy Mater.* **2014**, *4*, 1301465.
- (50) Yu, K.; Carter, E. A. A Strategy to Stabilize Kesterite CZTS for High-Performance Solar Cells. *Chem. Mater.* **2015**, *27*, 2920–2927.
- (51) Yu, K.; Carter, E. A. Determining and Controlling the Stoichiometry of Cu₂ZnSnS₄ Photovoltaics: The Physics and Its Implications. *Chem. Mater.* **2016**, *28*, 4415–4420.
- (52) Yu, K.; Carter, E. A. Elucidating Structural Disorder and the Effects of Cu Vacancies on the Electronic Properties of Cu₂ZnSnS₄. *Chem. Mater.* **2016**, *28*, 864–869.
- (53) Sai Gautam, G.; Senftle, T. P.; Carter, E. A. Understanding the Effects of Cd and Ag Doping in Cu₂ZnSnS₄ Solar Cells. *Chem. Mater.* **2018**, *30*, 4543–4555.
- (54) Mori, S.; Fukuda, S.; Sumikura, S.; Takeda, Y.; Tamaki, Y.; Suzuki, E.; Abe, T. Charge-Transfer Processes in Dye-Sensitized NiO Solar Cells. *J. Phys. Chem. C* **2008**, *112*, 16134–16139.
- (55) Zhu, H.; Hagfeldt, A.; Boschloo, G. Photoelectrochemistry of Mesoporous NiO Electrodes in Iodide/Triiodide Electrolytes. *J. Phys. Chem. C* **2007**, *111*, 17455–17458.
- (56) Hüfner, S. Electronic Structure of NiO and Related 3d-Transition-Metal Compounds. *Adv. Phys.* **1994**, *43*, 183–356.
- (57) Jang, W.-L.; Lu, Y.-M.; Hwang, W.-S.; Chen, W.-C. Electrical Properties of Li-Doped NiO Films. *J. Eur. Ceram. Soc.* **2010**, *30*, 503–508.
- (58) van Elp, J.; Eskes, H.; Kuiper, P.; Sawatzky, G. A. Electronic Structure of Li-Doped NiO. *Phys. Rev. B: Condens. Matter Mater. Phys.* **1992**, *45*, 1612–1622.
- (59) Yoshida, T.; Tanaka, T.; Yoshida, H.; Funabiki, T.; Yoshida, S. Study on the Dispersion of Nickel Ions in the NiO–MgO System by X-Ray Absorption Fine Structure. *J. Phys. Chem.* **1996**, *100*, 2302–2309.
- (60) Davies, P. K.; Navrotsky, A. Thermodynamics of Solid Solution Formation in NiO–MgO and NiO–ZnO. *J. Solid State Chem.* **1981**, *38*, 264–276.
- (61) Perdew, J. P.; Burke, K.; Ernzerhof, M. Generalized Gradient Approximation Made Simple. *Phys. Rev. Lett.* **1996**, *77*, 3865–3868.
- (62) Anisimov, V. I.; Zaanen, J.; Andersen, O. K. Band Theory and Mott Insulators: Hubbard U Instead of Stoner I. *Phys. Rev. B: Condens. Matter Mater. Phys.* **1991**, *44*, 943–954.
- (63) Anisimov, V. I.; Aryasetiawan, F.; Lichtenstein, A. I. First-Principles Calculations of the Electronic Structure and Spectra of Strongly Correlated Systems: The LDA + U Method. *J. Phys.: Condens. Matter* **1997**, *9*, 767–808.
- (64) Alidoust, N.; Toroker, M. C.; Carter, E. A. Revisiting Photoemission and Inverse Photoemission Spectra of Nickel Oxide from First Principles: Implications for Solar Energy Conversion. *J. Phys. Chem. B* **2014**, *118*, 7963–7971.
- (65) Zunger, A.; Wei, S.-H.; Ferreira, L. G.; Bernard, J. E. Special Quasirandom Structures. *Phys. Rev. Lett.* **1990**, *65*, 353–356.
- (66) Wei, S.-H.; Ferreira, L. G.; Bernard, J. E.; Zunger, A. Electronic Properties of Random Alloys: Special Quasirandom Structures. *Phys. Rev. B: Condens. Matter Mater. Phys.* **1990**, *42*, 9622–9649.
- (67) Borghs, G.; Bhattacharyya, K.; Deneffe, K.; Van Mieghem, P.; Mertens, R. Band-gap Narrowing in Highly Doped n - and p -type GaAs Studied by Photoluminescence Spectroscopy. *J. Appl. Phys.* **1989**, *66*, 4381–4386.
- (68) Kuiper, P.; Kruizinga, G.; Ghijssen, J.; Sawatzky, G. A.; Verweij, H. Character of Holes in $\text{Li}_x\text{Ni}_{1-x}\text{O}$ and Their Magnetic Behavior. *Phys. Rev. Lett.* **1989**, *62*, 221–224.
- (69) Wang, H.; Wei, W.; Hu, Y. H. NiO as an Efficient Counter Electrode Catalyst for Dye-Sensitized Solar Cells. *Top. Catal.* **2014**, *57*, 607–611.
- (70) Roessler, D. M.; Walker, W. C. Electronic Spectrum and Ultraviolet Optical Properties of Crystalline MgO. *Phys. Rev.* **1967**, *159*, 733–738.
- (71) van Elp, J.; Wieland, J. L.; Eskes, H.; Kuiper, P.; Sawatzky, G. A.; de Groot, F. M. F.; Turner, T. S. Electronic Structure of CoO, Li-Doped CoO, and LiCoO₂. *Phys. Rev. B: Condens. Matter Mater. Phys.* **1991**, *44*, 6090–6103.
- (72) Perdew, J. P. Orbital Functional for Exchange and Correlation: Self-Interaction Correction to the Local Density Approximation. *Chem. Phys. Lett.* **1979**, *64*, 127–130.
- (73) Perdew, J. P.; Zunger, A. Self-Interaction Correction to Density-Functional Approximations for Many-Electron Systems. *Phys. Rev. B: Condens. Matter Mater. Phys.* **1981**, *23*, 5048–5079.
- (74) Ritzmann, A. M.; Pavone, M.; Muñoz-García, A. B.; Keith, J. A.; Carter, E. A. Ab Initio DFT+U Analysis of Oxygen Transport in LaCoO₃: The Effect of Co³⁺ Magnetic States. *J. Mater. Chem. A* **2014**, *2*, 8060–8074.
- (75) Balberg, I.; Pinch, H. L. The Optical Absorption of Iron Oxides. *J. Magn. Magn. Mater.* **1978**, *7*, 12–15.
- (76) Kim, B.; Hong, S.; Lynch, D. W. Inverse-Photoemission Measurement of Iron Oxides on Polycrystalline Fe. *Phys. Rev. B: Condens. Matter Mater. Phys.* **1990**, *41*, 12227–12229.
- (77) Siegel, N. P.; Miller, J. E.; Ermanoski, I.; Diver, R. B.; Stechel, E. B. Factors Affecting the Efficiency of Solar Driven Metal Oxide Thermochemical Cycles. *Ind. Eng. Chem. Res.* **2013**, *52*, 3276–3286.
- (78) Anisimov, V. I.; Korotin, M. A.; Kurmaev, E. Z. Band-Structure Description of Mott Insulators (NiO, MnO, FeO, CoO). *J. Phys.: Condens. Matter* **1990**, *2*, 3973–3987.
- (79) Heyd, J.; Scuseria, G. E.; Ernzerhof, M. Hybrid Functionals Based on a Screened Coulomb Potential. *J. Chem. Phys.* **2003**, *118*, 8207–8215.
- (80) Kim, B.; Hong, S.; Lynch, D. W. Inverse-Photoemission Measurement of Iron Oxides on Polycrystalline Fe. *Phys. Rev. B: Condens. Matter Mater. Phys.* **1990**, *41*, 12227–12229.
- (81) Toroker, M. C.; Kanan, D. K.; Alidoust, N.; Isseroff, L. Y.; Liao, P.; Carter, E. A. First Principles Scheme to Evaluate Band Edge Positions in Potential Transition Metal Oxide Photocatalysts and Photoelectrodes. *Phys. Chem. Chem. Phys.* **2011**, *13*, 16644.
- (82) Kanan, D. K.; Carter, E. A. Ab Initio Study of Electron and Hole Transport in Pure and Doped MnO and MnO:ZnO Alloy. *J. Mater. Chem. A* **2013**, *1*, 9246.
- (83) Holstein, T. Studies of Polaron Motion. *Ann. Phys. (Amsterdam, Neth.)* **1959**, *8*, 325–342.
- (84) Holstein, T. Studies of Polaron Motion. *Ann. Phys. (Amsterdam, Neth.)* **1959**, *8*, 343–389.

- (85) Slack, G. A. Crystallography and Domain Walls in Antiferromagnetic NiO Crystals. *J. Appl. Phys.* **1960**, *31*, 1571–1582.
- (86) Dutta, T.; Gupta, P.; Gupta, A.; Narayan, J. Effect of Li Doping in NiO Thin Films on Its Transparent and Conducting Properties and Its Application in Heteroepitaxial P-n Junctions. *J. Appl. Phys.* **2010**, *108*, 083715.
- (87) Handley, S. J.; Bradberry, G. W. Estimates of Charge Carrier Mobility and Lifetime in Nickel Oxide. *Phys. Lett. A* **1972**, *40*, 277–278.
- (88) Shannon, R. D.; Prewitt, C. T. Effective Ionic Radii in Oxides and Fluorides. *Acta Crystallogr., Sect. B: Struct. Crystallogr. Cryst. Chem.* **1969**, *25*, 925–946.
- (89) Bosman, A. J.; van Daal, H. J. Small-Polaron versus Band Conduction in Some Transition-Metal Oxides. *Adv. Phys.* **1970**, *19*, 1–117.
- (90) Bransky, I.; Tannhauser, D. S. Mobility of Charge Carriers in Wüstite ($\text{FeO}1+\chi$). *Physica* **1967**, *37*, 547–552.
- (91) Gartstein, E.; Mason, T. O. Reanalysis of Wüstite Electrical Properties. *J. Am. Ceram. Soc.* **1982**, *65*, C-24–C-26.
- (92) Gavartin, J. L.; Shluger, A. L.; Catlow, C. R. A. Modelling of the Impurity-Vacancy Interaction in Magnesium Doped Lithium Oxide. *J. Phys.: Condens. Matter* **1993**, *5*, 7397–7408.
- (93) Mosey, N. J.; Liao, P.; Carter, E. A. Rotationally Invariant Ab Initio Evaluation of Coulomb and Exchange Parameters for DFT+U Calculations. *J. Chem. Phys.* **2008**, *129*, 014103.
- (94) Kanan, D. K.; Carter, E. A. Band Gap Engineering of MnO via ZnO Alloying: A Potential New Visible-Light Photocatalyst. *J. Phys. Chem. C* **2012**, *116*, 9876–9887.
- (95) Togo, A.; Tanaka, I. First Principles Phonon Calculations in Materials Science. *Scr. Mater.* **2015**, *108*, 1–5.
- (96) van de Walle, A.; Tiwary, P.; de Jong, M.; Olmsted, D. L.; Asta, M.; Dick, A.; Shin, D.; Wang, Y.; Chen, L.-Q.; Liu, Z.-K. Efficient Stochastic Generation of Special Quasirandom Structures. *CALPHAD: Comput. Coupling Phase Diagrams Thermochem.* **2013**, *42*, 13–18.
- (97) Goodwin, C. A.; Bowen, H. K.; Kingery, W. D. Phase Separation in the System (Fe,Mn)O. *J. Am. Ceram. Soc.* **1975**, *58*, 317–320.
- (98) Brahms, S.; Nikitine, S.; Dahl, J. P. On the Band Structure and the Absorption Spectrum of Cu_2O . *Phys. Lett.* **1966**, *22*, 31–33.
- (99) Zouaghi, M.; Prevot, B.; Carabatos, C.; Sieskind, M. Near Infrared Optical and Photoelectric Properties of Cu_2O . III. Interpretation of Experimental Results. *Phys. Status Solidi* **1972**, *11*, 449–460.
- (100) Wright, A. F.; Nelson, J. S. Theory of the Copper Vacancy in Cuprous Oxide. *J. Appl. Phys.* **2002**, *92*, 5849–5851.
- (101) Raebiger, H.; Lany, S.; Zunger, A. Origins of the P-Type Nature and Cation Deficiency in Cu_2O and Related Materials. *Phys. Rev. B: Condens. Matter Mater. Phys.* **2007**, *76*, 045209.
- (102) Scanlon, D. O.; Morgan, B. J.; Watson, G. W. Modeling the Polaronic Nature of P-Type Defects in Cu_2O : The Failure of GGA and GGA+U. *J. Chem. Phys.* **2009**, *131*, 124703.
- (103) Scanlon, D. O.; Morgan, B. J.; Watson, G. W.; Walsh, A. Acceptor Levels in P-Type Cu_2O : Rationalizing Theory and Experiment. *Phys. Rev. Lett.* **2009**, *103*, 096405.
- (104) Isseroff, L. Y.; Carter, E. A. Importance of Reference Hamiltonians Containing Exact Exchange for Accurate One-Shot GW Calculations of Cu_2O . *Phys. Rev. B: Condens. Matter Mater. Phys.* **2012**, *85*, 235142.
- (105) O’Keeffe, M.; Moore, W. J. Electrical Conductivity of Monocrystalline Cuprous Oxide. *J. Chem. Phys.* **1961**, *35*, 1324–1328.
- (106) Aggarwal, S.; Töpfer, J.; Tsai, T.-L.; Dieckmann, R. Point Defects and Transport in Binary and Ternary, Non-Stoichiometric Oxides. *Solid State Ionics* **1997**, *101–103*, 321–331.
- (107) Porat, O.; Riess, I. Defect Chemistry of Cu_{2-y}O at Elevated Temperatures. Part I: Non-Stoichiometry, Phase Width and Dominant Point Defects. *Solid State Ionics* **1994**, *74*, 229–238.
- (108) Tapiero, M.; Zielinger, J. P.; Noguet, C. Electrical Conductivity and Thermal Activation Energies in Cu_2O Single Crystals. *Phys. Status Solidi* **1972**, *12*, 517–520.
- (109) Fernando, C. A.; Wetthasinghe, S. Investigation of Photoelectrochemical Characteristics of N-Type Cu_2O Films. *Sol. Energy Mater. Sol. Cells* **2000**, *63*, 299–308.
- (110) Brown, I. D. What Factors Determine Cation Coordination Numbers? *Acta Crystallogr., Sect. B: Struct. Sci.* **1988**, *44*, 545–553.
- (111) Grossberg, M.; Krustok, J.; Raudoja, J.; Timmo, K.; Altosaar, M.; Raadik, T. Photoluminescence and Raman Study of $\text{Cu}_2\text{ZnSn}(\text{Se}_{x}\text{S}_{1-x})_4$ Monograins for Photovoltaic Applications. *Thin Solid Films* **2011**, *519*, 7403–7406.
- (112) Grossberg, M.; Krustok, J.; Raadik, T.; Kauk-Kuusik, M.; Raudoja, J. Photoluminescence Study of Disorder in the Cation Sublattice of $\text{Cu}_2\text{ZnSnS}_4$. *Curr. Appl. Phys.* **2014**, *14*, 1424–1427.
- (113) Grimme, S. Semiempirical GGA-Type Density Functional Constructed with a Long-Range Dispersion Correction. *J. Comput. Chem.* **2006**, *27*, 1787–1799.
- (114) Wang, G.; Zhao, W.; Cui, Y.; Tian, Q.; Gao, S.; Huang, L.; Pan, D. Fabrication of a $\text{Cu}_2\text{ZnSn}(\text{S},\text{Se})_4$ Photovoltaic Device by a Low-Toxicity Ethanol Solution Process. *ACS Appl. Mater. Interfaces* **2013**, *5*, 10042–10047.
- (115) Sanchez, J.; Ducastelle, F.; Gratias, D. Generalized Cluster Description of Multicomponent Systems. *Phys. A* **1984**, *128*, 334–350.
- (116) Chesman, A. S. R.; Embden, J. Van; Gaspera, E. Della; Du, N. W.; Webster, N. A. S.; Jasieniak, J. J. $\text{Cu}_2\text{ZnGeS}_4$ Nanocrystals from Air-Stable Precursors for Sintered Thin Film Alloys. *Chem. Mater.* **2014**, *26*, 5482–5491.
- (117) Redinger, A.; Berg, D. M.; Dale, P. J.; Siebentritt, S. The Consequences of Kesterite Equilibria for Efficient Solar Cells. *J. Am. Chem. Soc.* **2011**, *133*, 3320–3323.
- (118) Redinger, A.; Berg, D. M.; Dale, P. J.; Djemour, R.; Gütay, L.; Eisenbarth, T.; Valle, N.; Siebentritt, S. Route Toward High-Efficiency Single-Phase $\text{Cu}_2\text{ZnSn}(\text{S},\text{Se})_4$ Thin-Film Solar Cells: Model Experiments and Literature Review. *IEEE J. Photovoltaics* **2011**, *1*, 200–206.
- (119) Kofke, D. A.; Cummings, P. T. Quantitative Comparison and Optimization of Methods for Evaluating the Chemical Potential by Molecular Simulation. *Mol. Phys.* **1997**, *92*, 973–996.
- (120) Chen, S.; Walsh, A.; Gong, X.-G.; Wei, S.-H. Classification of Lattice Defects in the Kesterite $\text{Cu}_2\text{ZnSnS}_4$ and $\text{Cu}_2\text{ZnSnSe}_4$ Earth-Abundant Solar Cell Absorbers. *Adv. Mater.* **2013**, *25*, 1522–1539.
- (121) Fu, J.; Tian, Q.; Zhou, Z.; Kou, D.; Meng, Y.; Zhou, W.; Wu, S. Improving the Performance of Solution-Processed $\text{Cu}_2\text{ZnSn}(\text{S},\text{Se})_4$ Photovoltaic Materials by Cd^{2+} Substitution. *Chem. Mater.* **2016**, *28*, 5821–5828.
- (122) Qi, Y.-F.; Kou, D.-X.; Zhou, W.-H.; Zhou, Z.-J.; Tian, Q.-W.; Meng, Y.-N.; Liu, X.-S.; Du, Z.-L.; Wu, S.-X. Engineering of Interface Band Bending and Defects Elimination via a Ag-Graded Active Layer for Efficient $(\text{Cu},\text{Ag})_x\text{ZnSn}(\text{S},\text{Se})_4$ Solar Cells. *Energy Environ. Sci.* **2017**, *10*, 2401–2410.
- (123) Yan, C.; Sun, K.; Huang, J.; Johnston, S.; Liu, F.; Veettil, B. P.; Sun, K.; Pu, A.; Zhou, F.; Stride, J. A.; et al. Beyond 11% Efficient Sulfide Kesterite $\text{Cu}_2\text{Zn}_x\text{Cd}_{1-x}\text{SnS}_4$ Solar Cell: Effects of Cadmium Alloying. *ACS Energy Lett.* **2017**, *2*, 930–936.
- (124) Chen, S.; Yang, J.-H.; Gong, X. G.; Walsh, A.; Wei, S.-H. Intrinsic Point Defects and Complexes in the Quaternary Kesterite Semiconductor $\text{Cu}_2\text{ZnSnS}_4$. *Phys. Rev. B: Condens. Matter Mater. Phys.* **2010**, *81*, 245204.
- (125) Haxel, G. B.; Hedrick, J. B.; Orris, G. J. Fact Sheet 087-02 <https://pubs.usgs.gov/fs/2002/fs087-02/> (accessed Jul 15, 2018).
- (126) Sai Gautam, G.; Carter, E. A. Evaluating Transition Metal Oxides within DFT-SCAN and SCAN+U Frameworks for Solar Thermochemical Applications. *Phys. Rev. Mater.* **2018**, *2*, 095401.
- (127) Bendavid, L. I.; Carter, E. A. Status in Calculating Electronic Excited States in Transition Metal Oxides from First Principles. In *First Principles Approaches to Spectroscopic Properties of Complex*

Materials; Di Valentin, C., Botti, S., Cococcioni, M., Eds.; Springer: Berlin, Heidelberg, 2014; pp 47–98.

(128) Cramer, C. J.; Truhlar, D. G. Density Functional Theory for Transition Metals and Transition Metal Chemistry. *Phys. Chem. Chem. Phys.* **2009**, *11*, 10757.

(129) Harvey, J. N. On the Accuracy of Density Functional Theory in Transition Metal Chemistry. *Annu. Rep. Prog. Chem., Sect. C: Phys. Chem.* **2006**, *102*, 203.